

Characterization of fractional Chern insulator quasiparticles in moiré transition metal dichalcogenides

Zhao Liu,^{1,2,*} Bohao Li,^{3,†} and Fengcheng Wu^{3,4,‡}

¹*Zhejiang Institute of Modern Physics, Zhejiang University, Hangzhou 310058, China*

²*Zhejiang Key Laboratory of Micro-Nano Quantum Chips and Quantum Control, School of Physics, Zhejiang University, Hangzhou 310027, China*

³*School of Physics and Technology, Wuhan University, Wuhan 430072, China*

⁴*Wuhan Institute of Quantum Technology, Wuhan 430206, China*

(Dated: July 8, 2025)

We provide a detailed study of Abelian quasiparticles of valley polarized fractional Chern insulators (FCIs) residing in the top valence band of twisted bilayer MoTe₂ (tMoTe₂) at hole filling $\nu_h = 2/3$. We construct a tight-binding model of delocalized quasiparticles to capture the energy dispersion of a single quasiparticle. We then localize quasiparticles by short-range delta impurity potentials. Unlike the fractional quantum Hall (FQH) counterpart in the lowest Landau level (LLL), the density profile around the localized FCI quasiparticle in tMoTe₂ depends on the location of the impurity potential and loses the continuous rotation invariance. The FCI quasiparticle localized at moiré lattice center closely follows the anyon Wannier state of the tight-binding model of the mobile quasiparticle. Despite of the difference in density profiles, we find that the excess charge around the impurity potential for the $\nu_h = 2/3$ FCIs in tMoTe₂ is still similar to that of the $\nu = 2/3$ FQH state in the LLL if an effective magnetic length on the moiré lattice is chosen as the length unit, which allows a rough estimation of the spatial extent of the FCI quasiparticle. Far away from the impurity potential, this excess charge has the tendency to reach $e/3$, as expected for the Laughlin quasiparticle. The braiding phase of two FCI quasiparticles in tMoTe₂ also agrees with the theoretical prediction of fractional statistics. Based on the nearly ideal quantum geometry of the top valence band of tMoTe₂, we propose a trial wave function for localized FCI quasiparticles, which reproduces the key feature of the density profile around a quasiparticle. We also discuss the effect of band mixing on FCI quasiparticles in tMoTe₂.

I. INTRODUCTION

The nontrivial topology and enhanced electron-electron interactions in two-dimensional narrow bands with nonzero Chern number have given rise to various novel correlated phases of matters. As a representative example, interacting particles partially occupying a nearly flat topological band can form zero-field analogues of the celebrated fractional quantum Hall (FQH) effect [1, 2] at suitable filling factors, dubbed fractional Chern insulators (FCIs) [3–10]. A main trend in the recent development of this field is to gather inspiration from material science to look for lattice platforms that can really produce FCIs. Remarkably, FCIs were theoretically predicted to exist in van-der-Waals heterostructures with moiré patterns [11–17]. Consistent with these theoretical predictions, experiments have reported observations of FCIs in rhombohedral graphene aligned with hexagonal boron nitride [18–23] and twisted homobilayer MoTe₂ (tMoTe₂) [24–31]. Further theoretical studies flourish to understand the exciting experimental results [32–50].

While exhibiting notable differences from FQH states, FCIs carry intrinsic topological orders [51] like their FQH cousins. The defining features of an intrinsic topological order include the quantized Hall resistance, topological ground-state degeneracy [52] and fractionalized quasiparticle excitations called anyons [2, 53, 54]. On the one hand, the energy cost of creat-

ing these quasiparticles determines the stability of FCI ground states and is closely related to the temperature dependence of the longitudinal resistance measured in experiments. On the other hand, the direct characterization of quasiparticles, including their spatial extension, charge, statistics, and interaction, is highly relevant to the investigations of anyons using interferometers [55–63], anyon collider [64, 65], scanning tunneling microscope (STM) [66], and optical imaging [67]. In the context of FCIs, the energy gaps of various fractionalized excitations have been systematically studied for the FCIs at hole filling $\nu_h = 2/3$ in tMoTe₂ [68]. However, the characterization of (localized) FCI quasiparticles is mostly limited in toy tight-binding models [69–78]. To our knowledge, there has not been a previous attempt of a microscopic characterization of quasiparticles in moiré materials where FCIs were recently observed in experiments.

In this work, we present a detailed numerical characterization of the Abelian quasiparticles of $\nu_h = 2/3$ FCIs in tMoTe₂. We adopt the continuum model of tMoTe₂ and focus on experimentally realistic twist angles near 4° . In the presence of interactions, the many-body calculations are mostly carried out using extensive exact diagonalization (ED) under the assumption of valley polarization and single-band projection. First of all, we find that the hole’s real-space density of the FCI ground state, unlike its FQH counterpart, is strongly modulated within a moiré unit cell, while the total hole numbers in different unit cells remains identical. The density non-uniformness can be interpreted by the confinement of holes in specific regions of the moiré lattice. We then create quasiparticles in the FCI ground state and construct an effective tight-binding model to describe the dispersion of a single mobile

* zhaol@zju.edu.cn

† bohaoli@whu.edu.cn

‡ wufcheng@whu.edu.cn

quasiparticle. This dispersion, together with the spectrum of two mobile quasiparticles, can be used to estimate the interaction between two quasiparticles, which may predict whether bunches of two quasiparticles occurs. Supposing holes interact via the weakly screened Coulomb potential, we find signature of repulsive interactions between mobile quasiparticles.

On the other hand, we study the FCI quasiparticles localized by delta impurity potentials. The density profile around a single localized quasiparticle varies with the location of the impurity potential, and is well described by the anyon Wannier states constructed from the tight-binding model of the mobile quasiparticle. The nearly ideal quantum geometry [79–82] of the top valence band of tMoTe₂ allows a variational construction of trial wave functions of FCI anyons. Monte Carlo simulation using these trial wave functions reproduce the key features of the density profile around a localized quasiparticle obtained by ED, thus justifying the validity of trial wave functions. We also estimate the charge of a localized quasiparticle and the braiding statistics of two localized quasiparticles in tMoTe₂. The results are consistent with theoretical expectations for the $\nu = 2/3$ Laughlin state, i.e., fractional charge of $e/3$ and braiding phase $-2\pi/3$. However, the largest system size within the capability of ED is still insufficient for the full development of a quasiparticle. If the effective lattice magnetic length $\ell_0 \equiv \sqrt{S_{\text{uc}}/(2\pi)}$ (S_{uc} is the area of moiré unit cell) [69] and the magnetic length ℓ_B are used as the length units in tMoTe₂ and the lowest Landau level (LLL), respectively, the accumulated excess charge around the impurity potential in tMoTe₂ looks similar to that of the $\nu = 2/3$ FQH state in the LLL, but shows slower damping with increasing distance. We estimate the quasiparticle radius of the $\nu = 2/3$ FQH state in the LLL as $4 - 6\ell_B$ by analyzing the density profile and the braiding phase. This suggests an estimation of the spatial extent of a localized $\nu_h = 2/3$ FCI quasiparticle in tMoTe₂ as $6\ell_0$, which is 120 \AA at twist angle 3.7° . This result could be further increased once band mixing is considered.

The remaining part of this paper is organized as follows. In Sec. II, we characterize the quasiparticle of the $\nu = 2/3$ FQH state in the LLL for later comparison with the FCI case. In Sec. III, we introduce the continuum model of tMoTe₂, and show the density of the $\nu_h = 2/3$ FCI ground states. In Sec. IV, we construct the tight-binding model of mobile quasiparticles of $\nu_h = 2/3$ FCIs in tMoTe₂, then describe the numerical characterization of localized quasiparticles. Trial wave functions for FCI anyons and their Monte Carlo simulations are discussed in Sec. V. Finally, we summarize our results in Sec. VI. More numerical data are presented in the Appendix.

II. FQH QUASIPARTICLES AT $\nu = 2/3$ IN THE LLL

Before studying the $\nu_h = 2/3$ FCI quasiparticles in tMoTe₂, we first characterize quasiparticles of the conventional FQH state at $\nu = 2/3$ in the LLL, for the sake of comparing quasiparticle physics in moiré flat bands and in the LLL. Note that we will focus on $\nu = 2/3$ quasiparticles rather than quasiholes. We find that ED cannot deal with the latter

in finite systems due to its too large spatial extent.

A. Model of the LLL

We consider N interacting fermions of charge e on a square torus of length L penetrated by a uniform perpendicular magnetic field B . The number of flux quanta, N_ϕ , through the surface of the torus is an integer satisfying $L^2 = 2\pi\ell_B^2 N_\phi$, where $\ell_B = \sqrt{\hbar/(eB)}$ is the magnetic length. The filling factor is defined as $\nu = N/N_\phi$. In a strong magnetic field, we can restrict all fermions in the LLL, such that the kinetic energy is simply a constant. In this case, the effective part in the many-body Hamiltonian is just the (two-body) interaction between fermions, which takes the form of

$$H_{\text{int}} = \sum_{m_1, \dots, m_4=0}^{N_\phi-1} V_{m_1, m_2, m_3, m_4} c_{m_1}^\dagger c_{m_2}^\dagger c_{m_3} c_{m_4}. \quad (1)$$

Here c_m^\dagger (c_m) creates (annihilates) a fermion in the m th LLL orbital, whose wave function is $\psi_m(x, y) = \left(\frac{1}{\sqrt{\pi L \ell_B}}\right)^{1/2} \sum_{n=-\infty}^{+\infty} e^{i\frac{2\pi}{L}(m+nN_\phi)y} e^{-\frac{1}{2\ell_B^2} \left[x - \frac{2\pi}{L}\ell_B^2(m+nN_\phi)\right]^2}$ under the Landau gauge. The interaction matrix element is

$$V_{\{m_i\}} = \frac{1}{2} \delta_{m_1+m_2, m_3+m_4}^{\text{mod } N_\phi} \sum_{s, t=-\infty}^{+\infty} \delta_{t, m_1-m_4}^{\text{mod } N_\phi} \times V(\mathbf{q}) e^{-\frac{1}{2}|\mathbf{q}|^2 \ell_B^2} e^{i\frac{2\pi s}{N_\phi}(m_1-m_3)}, \quad (2)$$

where $\delta_{i,j}^{\text{mod } N_\phi}$ is the periodic Kronecker delta function with period N_ϕ , $\mathbf{q} = (q_x, q_y) = \frac{2\pi}{L}(s, t)$, and $V(\mathbf{q})$ is the Fourier transform of the interaction potential. We consider the realistic dual-gate setup and choose the screened Coulomb potential $V(\mathbf{q}) = \frac{e^2}{4\pi\epsilon\epsilon_0} \frac{1}{L^2} \frac{2\pi \tanh(|q|d)}{|q|}$ for the interaction, where ϵ is the relative dielectric constant of the material and d is the distance from the top (or bottom) gate to the two-dimensional electron gas. We set $d = 5\ell_B$ (weak screening) throughout our calculations in this section. The results are not sensitive to the precise value of d so long as the screening is not too strong.

The ground state of the gate-screened Coulomb interaction at $\nu = 2/3$ is approximately the particle-hole conjugate of the celebrated Laughlin model state, with three-fold topological degeneracy on the torus and Abelian quasiparticle excitations. To generate N_{qp} quasiparticles in the ground state, we add N_{qp} magnetic fluxes and N_{qp} fermions to the system, leading to $N_\phi = \frac{1}{2}(3N - N_{\text{qp}})$. We consider the cases with sufficiently dilute quasiparticles, such that the charge gap of the finite system remains open. In principle, we should diagonalize the full Hamiltonian $H_{\text{int}} + \sum_{j=1}^{N_{\text{qp}}} U_{\text{imp}}(\mathbf{w}_j)$ to get states with localized quasiparticles, where $U_{\text{imp}}(\mathbf{w})$ is an attractive impurity potential aiming to pin a quasiparticle at the specific position \mathbf{w} . However, localized quasiparticles break the translation invariance on the torus, making this direct diagonalization computationally expensive.

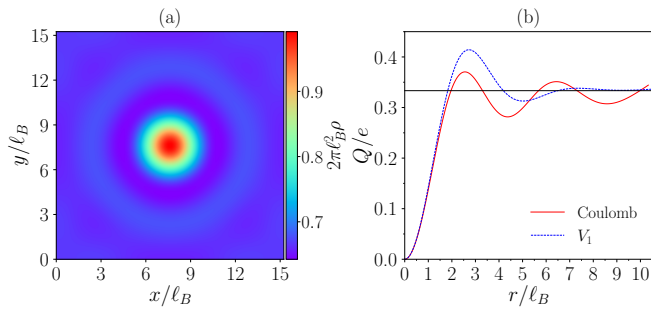


Figure 1. (a) The density distribution for a single-quasiparticle excitation of the $\nu = 2/3$ fermionic FQH state on a square torus with $N = 25, N_s = 37$. (b) The excess charge around the impurity potential. The horizontal reference line indicates $Q = e/3$. The dashed line in (b) is obtained using the first-order Haldane's pseudopotential. Otherwise the interaction is the screened Coulomb potential.

Fortunately, as long as the charge gap of the system remains finite, the energy spectrum of H_{int} always contains a low-energy subspace, corresponding to N_{qp} delocalized quasiparticles. The dimension of this subspace can be predicted by Haldane's exclusion principle [83] or the conformal field theory [84]. Assuming that the impurity potentials only mix states within this low-energy subspace without coupling them to higher excited levels, we first diagonalize H_{int} to obtain the states of delocalized quasiparticles, then diagonalize the impurity potentials in the corresponding subspace to localize quasiparticles. The advantage of this two-step method is that the translation invariance is still available in the first step to reduce the many-body Hilbert space dimension. For the $\nu = 2/3$ Coulomb ground state, we find an attractive δ impurity potential $U_{\text{imp}}(\mathbf{w}) = -U_0 \sum_{i=1}^N \delta(\mathbf{r}_i - \mathbf{w})$, where \mathbf{r}_i is the position of the i th fermion and $U_0 > 0$, can readily pin a quasiparticle at \mathbf{w} . The second quantization form of such an impurity potential projected to the LLL is

$$U_{\text{imp}}(\mathbf{w}) = -U_0 \sum_{m_1, m_2=0}^{N_\phi} [\psi_{m_1}^*(\mathbf{w}) \psi_{m_2}(\mathbf{w})] c_{m_1}^\dagger c_{m_2}. \quad (3)$$

B. Single quasiparticle

We set $N_\phi = \frac{1}{2}(3N - 1)$ to generate a single quasiparticle excitation in the $\nu = 2/3$ Coulomb ground state. In this case, the low-energy subspace of H_{int} corresponding to a delocalized quasiparticle contains N_ϕ states. Without loss of generality, we put the single impurity potential at the center of the torus. After diagonalizing the impurity potential in the quasiparticle subspace of dimension N_ϕ , we obtain three nearly degenerate ground states, over which we compute the average real-space density distribution $\rho(\mathbf{r})$ of fermions. Note that the density profile of the $\nu = 2/3$ quasiparticle can be related to that of the $\nu = 1/3$ quasihole by the particle-hole transformation, which is guaranteed by the particle-hole symmetry within the LLL.

In Fig. 1, we display the results for the largest system size,

$N = 25, N_\phi = 37$, that we can reach using ED. There is a pronounced peak at the location of the impurity potential [Fig. 1(a)]. To verify that the density peak corresponds to a localized quasiparticle, we compute the excess charge defined as

$$Q(r) = e \int_{S_r} [\rho(\mathbf{r}') - \rho_0(\mathbf{r}')] d^2 \mathbf{r}', \quad (4)$$

where the area integral is over the disk S_r of radius r centered at the impurity potential, and $\rho_0(\mathbf{r})$ is the density of the $\nu = 2/3$ ground state without quasiparticles. In the FQH case, we simply have uniform $\rho_0 = \nu/(2\pi\ell_B^2)$. Using the fact that $\rho(\mathbf{r})$ is isotropic around the impurity potential, we can simplify the excess charge as $Q(r) = 2\pi e \int_0^r [\rho(r') - \rho_0] r' dr'$, where $\rho(r)$ is the density distribution along the diagonal direction of the sample. One can see that $Q(r)$ oscillates around $e/3$ when $r \gtrsim 2\ell_B$ [Fig. 1(b)]. Moreover, the oscillation amplitude decays with increasing r . While larger system sizes are still needed for the full convergence of excess charge, our results provide compelling evidence that a $e/3$ quasiparticle is localized by the impurity potential at the sample center, which is consistent with the Abelian $\nu = 2/3$ quasiparticle.

One method to estimate the radius R_{qp} of the spatial extent of a quasiparticle is to utilize the second moment of the radial density $\rho(r)$ [69, 74, 85], defined as

$$R_{\text{qp}} = \sqrt{\frac{\int_0^{r_{\text{max}}} |\rho(r) - \rho(r_{\text{max}})| r^3 dr}{\int_0^{r_{\text{max}}} |\rho(r) - \rho(r_{\text{max}})| r dr}}, \quad (5)$$

where r_{max} is the largest distance from the torus center. A numerical calculation of Eq. (5) for the system size in Fig. 1 shows $R_{\text{qp}} \approx 4\ell_B$. If we replace the Coulomb interaction with the short-range first-order Haldane's pseudopotential [86], we get $R_{\text{qp}} \approx 2.6\ell_B$. The smaller spatial extent of the quasiparticle for the pseudopotential interaction can also be seen in the excess charge [dashed lines in Fig. 1(b)], which almost converges to $e/3$ for the same system size.

C. Braiding of two quasiparticles

Fractional braiding statistics is another defining feature of quasiparticles. For simplicity, we generate two quasiparticles and use two impurities to pin and separate them. In this case, we again obtain three nearly degenerate ground states after diagonalizing the impurity potentials in the subspace of two delocalized quasiparticles. In order to braid these two quasiparticles, we fix the position of one impurity potential at the torus center and slowly dragging the other counterclockwise along a circle of radius D around the torus center. The Berry phase accumulated during this process is encoded in the unitary matrix

$$\mathcal{B} = \exp \left\{ i \int_0^{2\pi} \gamma(\theta) d\theta \right\}, \quad (6)$$

where θ is the polar angle of the mobile impurity potential, $\gamma_{nn'}(\theta) = i \langle \psi_n(\theta) | \nabla_\theta | \psi_{n'}(\theta) \rangle$ is the Berry connection matrix, and $\{|\psi_n(\theta)\rangle\}$ are the three ground states for

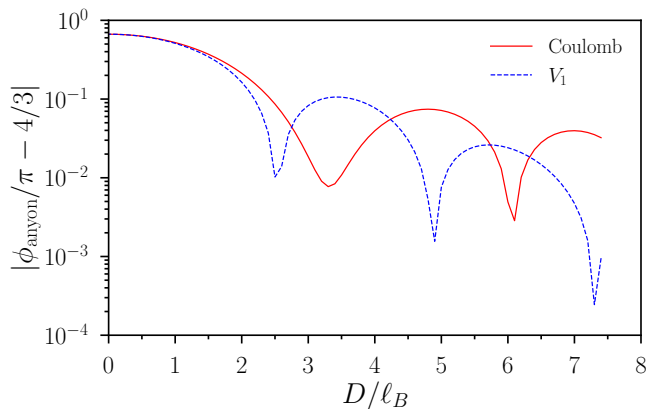


Figure 2. The fractional statistical phase versus the distance between two quasiparticles for the $\nu = 2/3$ fermionic FQH state on a square torus with $N = 24, N_\phi = 35$. The interaction potentials are screened Coulomb and the first-order Haldane's pseudopotential for the solid and dashed lines, respectively.

the configuration of impurity potentials at a specific θ . To remove the phase ambiguity in the states returned by numerical diagonalization, we impose a smooth gauge condition $\langle \psi_n(\theta) | \psi_{n'}(\theta + d\theta) \rangle = \delta_{nn'} + \mathcal{O}(d\theta^2)$, which leads to $\mathcal{B}_{nn'} = \langle \psi_n(0) | \psi_{n'}(2\pi) \rangle$. The eigenvalues of the 3×3 matrix \mathcal{B} are $(e^{ip_1}, e^{ip_2}, e^{ip_3})$, where p_1, p_2 , and p_3 are the Berry phases. We find that their numerical values are very close to each other, so we average over them.

The total Berry phase can be split into two parts: one is the Aharonov-Bohm (AB) phase caused by moving a single quasiparticle in the uniform magnetic field along the same path without the other quasiparticle enclosed; and the other comes from the fractional statistics between two quasiparticles. The AB phase p_i^{AB} should be $(\pi/3)(D/\ell_B)^2$, which we have numerically confirmed. Then we obtain the three fractional statistical phases as $p_i^{\text{anyon}} = p_i - p_i^{\text{AB}}$. Their averaged value ϕ_{anyon} is displayed in Fig. 2 as a function of D for $N = 24, N_\phi = 35$, which is the largest system size we can reach in the presence of two quasiparticles.

When D is large enough, we expect that ϕ_{anyon} exponentially converges to the theoretical value $4\pi/3$ (equivalently, $-2\pi/3$). However, as shown in Fig. 2, the deviation from this theoretical value still oscillates around $10^{-2}\pi$ even in the largest system size for the farthest separations between two quasiparticles. Therefore, bigger samples are required to further reduce this deviation. The critical value of D at which ϕ_{anyon} is close enough to the theoretical value can be used as another estimation of quasiparticle size. We set a threshold 10^{-2} for the revival in the oscillations of $|\phi_{\text{anyon}}/\pi - 4/3|$. Using an exponential fitting for the first two revivals, we predict the critical $D \approx 12\ell_B$, which gives the quasiparticle radius as $R_{\text{qp}} \approx 6\ell_B$. Compared with the Coulomb case, the pseudopotential leads to faster convergence of the fractional statistical phase (Fig. 2), suggesting $R_{\text{qp}} \approx 3.5\ell_B$.

III. TWISTED BILAYER MOTE₂

Now we turn to FCIs in tMoTe₂. We will first introduce the model, then present the density of particles in the FCI ground state without quasiparticles.

A. Model of tMoTe₂

The moiré superlattice consists of two MoTe₂ monolayers of lattice constant $a = 3.52 \text{ \AA}$, with a twist angle θ in between. At small twist angles, the lattice constant of the moiré pattern is $a_M \approx a/\theta \gg a$. Accordingly, the monolayer Brillouin zone is folded into the much smaller moiré Brillouin zone (MBZ). There are three high-symmetry positions in each moiré unit cell: $\mathcal{R}_M^M, \mathcal{R}_M^X$ and \mathcal{R}_X^M , where M and X represent metal and chalcogen atoms, respectively. \mathcal{R}_α^β stands for the local configuration in which α atom in the bottom layer is vertically aligned with the β atom in the top layer. We choose the primitive moiré lattice vectors as $\mathbf{a}_1 = (\frac{\sqrt{3}}{2}, \frac{1}{2})a_M$ and $\mathbf{a}_2 = (-\frac{\sqrt{3}}{2}, \frac{1}{2})a_M$. In the reciprocal space, the K and K' valleys are separated by a large momentum difference at small twist angles θ , such that they can be considered independently. Moreover, spin is effectively locked to valley due to the strong spin-orbit coupling near the two valleys.

We follow a continuum description of the low-energy valence bands of tMoTe₂ in the K and K' valley [87]. Since FCIs were experimentally observed when the top moiré valence bands are doped by holes, it is natural to work in the hole picture. The effective single-hole continuum Hamiltonian (in the K valley) takes the form of

$$H_{0,K}(\mathbf{r}) = - \begin{pmatrix} h_b(\mathbf{r}) + \Delta_b(\mathbf{r}) & \Delta_T^\dagger(\mathbf{r}) \\ \Delta_T(\mathbf{r}) & h_t(\mathbf{r}) + \Delta_t(\mathbf{r}) \end{pmatrix} \quad (7)$$

in the layer basis, with t and b denoting the top and bottom layer, respectively. The Hamiltonian $H_{0,K}(\mathbf{r})$ differs from that in Ref. [87] by a particle-hole transformation. Here $h_l(\mathbf{r}) = -\hbar(+i\nabla - \mathbf{K}_l)^2/(2m^*)$ describes the quadratic valence band edge of monolayer MoTe₂, where $m^* = 0.6m_e$ is the effective mass and \mathbf{K}_l is the K point of layer l . Each layer feels a moiré potential $\Delta_l(\mathbf{r}) = 2v \sum_{j=1,3,5} \cos(\mathbf{G}_j \cdot \mathbf{r} + l\phi)$, where $\mathbf{G}_j = \frac{4\pi}{\sqrt{3}a_M} (\cos(\frac{\pi}{3}(j-1)), \sin(\frac{\pi}{3}(j-1)))$ are the shortest moiré reciprocal lattice vectors, and l is $+1$ (-1) for the bottom (top) layer. The interlayer tunneling $\Delta_T(\mathbf{r}) = w(1 + e^{-i\mathbf{G}_2 \cdot \mathbf{r}} + e^{-i\mathbf{G}_3 \cdot \mathbf{r}})$. Both the intralayer moiré potential and the interlayer tunneling are approximated by first harmonic expansion. Throughout our work, we adopt $(v, \phi, w) = (20.8 \text{ meV}, +107.7^\circ, -23.8 \text{ meV})$ [37], which were obtained by recent first-principles calculations for θ near 4° . The single-particle Hamiltonian in the K' valley can be determined by time reversal conjugate of $H_{0,K}(\mathbf{r})$.

To get the moiré band structure, we need to further transform $H_{0,K}(\mathbf{r})$ to the momentum space. For convenience we choose the center of the MBZ in the K valley as the origin of the k -space. Under the plane-wave basis, the result is

$$\begin{aligned}
H_{0,K} = & - \sum_{\mathbf{k}} \left\{ \sum_{l=t,b} h_l(-\mathbf{k} - \mathbf{K}_l) c_{K,l,\mathbf{k}}^\dagger c_{K,l,\mathbf{k}} + v \sum_{l=t,b} \sum_{j=1,3,5} \left(e^{il\phi} c_{K,l,\mathbf{k}+\mathbf{G}_j}^\dagger c_{K,l,\mathbf{k}} + \text{h.c.} \right) \right. \\
& \left. + w \left(c_{K,b,\mathbf{k}}^\dagger c_{K,t,\mathbf{k}} + c_{K,b,\mathbf{k}+\mathbf{G}_2}^\dagger c_{K,t,\mathbf{k}} + c_{K,b,\mathbf{k}+\mathbf{G}_3}^\dagger c_{K,t,\mathbf{k}} + \text{h.c.} \right) \right\}, \quad (8)
\end{aligned}$$

where $c_{K,l,\mathbf{k}}^\dagger$ creates a hole with wave vector \mathbf{k} in valley K and layer l . The monolayer Hamiltonian is $h_l(-\mathbf{k} - \mathbf{K}_l) = -\frac{\hbar^2 |-\mathbf{k} - \mathbf{K}_l|^2}{2m^*}$. For each point \mathbf{k}_0 in the MBZ of the K valley, we let $\mathbf{k} = \mathbf{k}_0 + m_1 \mathbf{G}_1 + m_2 \mathbf{G}_2$ in Eq. (8). With truncations $m_1, m_2 = -M, \dots, M$ (we choose $M = 7$ in our calculations), $H_{0,K}$ can be constructed as a matrix of dimension $2(2M+1)^2$ under the plane-wave basis $|K, l, \mathbf{k}\rangle \equiv c_{K,l,\mathbf{k}}^\dagger |\text{vac}\rangle$. The eigenvalues E_{K,n,\mathbf{k}_0} of this matrix give the hole band energies at \mathbf{k}_0 , with n the band index. The band eigenvectors can be expressed as $|K, n, \mathbf{k}_0\rangle = \sum_{l,m_1,m_2} u_{l,m_1,m_2}^{K,n,\mathbf{k}_0} |K, l, \mathbf{k}_0 + m_1 \mathbf{G}_1 + m_2 \mathbf{G}_2\rangle$. In real space, the corresponding Bloch state is a layer spinor

$$\psi_{K,n,\mathbf{k}_0}(\mathbf{r}) = \frac{1}{\sqrt{\mathcal{A}}} \begin{pmatrix} \sum_{\mathbf{G}} e^{i(\mathbf{k}_0+\mathbf{G})\cdot\mathbf{r}} u_{t,m_1,m_2}^{K,n,\mathbf{k}_0} \\ \sum_{\mathbf{G}} e^{i(\mathbf{k}_0+\mathbf{G})\cdot\mathbf{r}} u_{b,m_1,m_2}^{K,n,\mathbf{k}_0} \end{pmatrix}, \quad (9)$$

where \mathcal{A} is the area of the system and $\mathbf{G} = m_1 \mathbf{G}_1 + m_2 \mathbf{G}_2$. The band structure E_{K',n,\mathbf{k}_0} and $|K', n, \mathbf{k}_0\rangle$ can be obtained similarly for the K' valley. For the model parameters we choose, the top valence band in each valley is isolated and relatively flat. The valence bands in different valleys carry opposite Chern number $\mathcal{C} = \pm 1$. The second valence band in each valley is also isolated and topological, whose Chern number is opposite to that of the top valence band.

Given the moiré band structure, the whole many-body Hamiltonian of holes in tMoTe₂, including the band dispersion, the two-body density-density interaction of holes, and the impurity potential, can be expressed in the basis of hole bands $|\eta, n, \mathbf{k}\rangle$ as

$$\begin{aligned}
H = & \sum_{\mathbf{k}} \sum_{\eta,n}^{\text{MBZ}} E_{\eta,n,\mathbf{k}} \gamma_{\eta,n,\mathbf{k}}^\dagger \gamma_{\eta,n,\mathbf{k}} \\
& + \sum_{\{\mathbf{k}_i\}} \sum_{\eta,\eta'}^{\text{MBZ}} \sum_{\{n_i\}} V_{\{\mathbf{k}_i\}\{n_i\}}^{(\eta\eta')} \gamma_{\eta,n_1,\mathbf{k}_1}^\dagger \gamma_{\eta',n_2,\mathbf{k}_2}^\dagger \gamma_{\eta',n_3,\mathbf{k}_3} \gamma_{\eta,n_4,\mathbf{k}_4} \\
& + \sum_{\{\mathbf{k}_i\}} \sum_{\eta}^{\text{MBZ}} \sum_{\{n_i\}} U_{\{\mathbf{k}_i\}\{n_i\}}^\eta \gamma_{\eta,n_1,\mathbf{k}_1}^\dagger \gamma_{\eta,n_2,\mathbf{k}_2}, \quad (10)
\end{aligned}$$

where all wave vectors are restricted in the MBZ, and $\gamma_{\eta,n,\mathbf{k}}^\dagger$ creates a hole with wave vector \mathbf{k} in band n of valley η , i.e., $|\eta, n, \mathbf{k}\rangle = \gamma_{\eta,n,\mathbf{k}}^\dagger |\text{vac}\rangle$. We have assumed that the impurity potential does not flip spins. As a result of spin-valley locking in tMoTe₂, the impurity potential does not couple the two valleys and the number of holes in each valley is conserved. The interaction matrix element $V_{\{\mathbf{k}_i\}\{n_i\}}^{(\eta\eta')} = \frac{1}{2} \delta'_{\mathbf{k}_1+\mathbf{k}_2,\mathbf{k}_3+\mathbf{k}_4} \sum_{\mathbf{G}} V(\mathbf{k}_1 - \mathbf{k}_4 + \mathbf{G}) M_{\eta,n_1,n_4}(\mathbf{k}_1, \mathbf{k}_4 -$

$\mathbf{G}) M_{\eta',n_2,n_3}(\mathbf{k}_2, \mathbf{k}_3 + \mathbf{G} + \delta\mathbf{G})$, where δ' is the 2D periodic Kronecker delta function with period of primitive moiré reciprocal lattice vectors, $V(\mathbf{q})$ is the Fourier transform of the interaction potential of holes, \mathbf{G} is a reciprocal lattice vector, $M_{\eta,n,n'}(\mathbf{k}, \mathbf{k}') \equiv \sum_{l,m_1,m_2} [u_{l,m_1,m_2}^{\eta,n,\mathbf{k}}]^* u_{l,m_1,m_2}^{\eta',n',\mathbf{k}'}$, and $\delta\mathbf{G} = \mathbf{k}_1 + \mathbf{k}_2 - \mathbf{k}_3 - \mathbf{k}_4$. Here we adopt the gauge that $\psi_{\eta,n,\mathbf{k}_0+\mathbf{G}}(\mathbf{r}) = \psi_{\eta,n,\mathbf{k}_0}(\mathbf{r})$ for any reciprocal lattice vector \mathbf{G} . Therefore, $u_{l,m_1,m_2}^{\eta,n,\mathbf{k}_0+\mathbf{G}'} = u_{l,m_1+m_1',m_2+m_2'}^{\eta,n,\mathbf{k}_0}$, where $\mathbf{G}' = m_1' \mathbf{G}_1 + m_2' \mathbf{G}_2$. In the following, we still choose $V(\mathbf{q}) = \frac{e^2}{4\pi\epsilon_0} \frac{1}{\mathcal{A}} \frac{2\pi \tanh(|\mathbf{q}|d)}{|\mathbf{q}|}$, as in the FQH case. The matrix element of the impurity potential is $U_{\{\mathbf{k}_i\}\{n_i\}}^\eta = \sum_{\mathbf{G}} U(\mathbf{k}_1 - \mathbf{k}_2 + \mathbf{G}) M_{\eta,n_1,n_2}(\mathbf{k}_1, \mathbf{k}_2 - \mathbf{G})$, where $U(\mathbf{q})$ is the Fourier transform of the impurity potential. For numerical efficiency, one has to project Eq. (10) to a finite set of bands. The experimental observations of valley polarized FCIs at hole filling $\nu_h = 2/3$ have been supported by single-band ED that only keeps the top valence band in a single valley [37, 38]. ED calculations that keep both valleys and two bands per valley also indicate that the $\nu_h = 2/3$ FCIs still survive in a small region of the (θ, ϵ) parameter space [40].

B. Density of holes in FCI ground states

Before exploring quasiparticles, we first examine the real-space density of holes in the absence of quasiparticles for the valley polarized $\nu_h = 2/3$ FCI ground states. The system size is labeled by the number of holes N and the number of moiré unit cells N_s . For a general valley polarized ground state, the real-space density is

$$\rho(\mathbf{r}) = \sum_{\eta,n,n',\mathbf{k},\mathbf{k}'} \langle \gamma_{\eta,n,\mathbf{k}}^\dagger \gamma_{\eta,n',\mathbf{k}'} \rangle \psi_{\eta,n,\mathbf{k}}^*(\mathbf{r}) \psi_{\eta,n',\mathbf{k}'}(\mathbf{r}), \quad (11)$$

where the expectation $\langle \cdot \rangle$ is over the ground state. The restriction $\mathbf{k} = \mathbf{k}'$ is imposed if the ground state has translation symmetry. We project Eq. (10) to the top valence band of valley K , and calculate the density averaged over the three $\nu_h = 2/3$ ground states at twist angle $\theta = 3.7^\circ$. In this case, the real-space density can be simplified to $\rho(\mathbf{r}) = \sum_{\mathbf{k}} n_{\mathbf{k}} |\psi_{\mathbf{k}}(\mathbf{r})|^2$, where $n_{\mathbf{k}}$ is the momentum-space occupation of holes and $\psi_{\mathbf{k}}(\mathbf{r})$ is the wavefunction of the single band. To make finite-size systems as isotropic as possible, we apply ED to samples satisfying tilted geometry [88, 89]. The sample details used in this work are given in Appendix A.

Unlike the FQH case, the real-space density of moiré FCIs is not uniform, as shown in Fig. 3(a). $\rho(\mathbf{r})$ is strongly peaked near the \mathcal{R}_M^X and \mathcal{R}_X^M positions, but almost vanishes near the

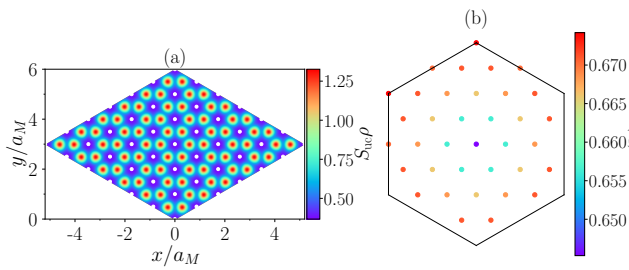


Figure 3. (a) The real-space density of holes for the $\nu_h = 2/3$ FCI ground state in tMoTe₂. The system size is $N = 24, N_s = 36$. The white dots indicate the \mathcal{R}_M^M positions. In (b), we show the momentum-space occupation for the system in (a). We set $\theta = 3.7^\circ$, $d = 10$ nm and $\epsilon = 10$.

\mathcal{R}_M^M points. As the hole occupation in the momentum space is approximately uniform [Fig. 3(b)], this non-uniform $\rho(\mathbf{r})$ is determined by the real-space distribution of single-particle band wave functions. As shown in Ref. [90], the holes in the top valence band indeed tend to be confined near the \mathcal{R}_M^X and \mathcal{R}_X^M positions when the first two valence bands carry Chern number $\mathcal{C} = \pm 1$, which holds for the parameters chosen by us. In this case, the first two valence bands in the K valley can be approximated by the Haldane model on an effective honeycomb lattice formed by \mathcal{R}_M^X and \mathcal{R}_X^M sites. We emphasize that the density non-uniformity only occurs in the length scale of one moiré unit cell for the FCI ground states. After summing the density within a moiré unit cell, we get the same total particle number $n_{\text{uc}} = |\nu|/S_{\text{uc}}$ for all unit cells, where S_{uc} is the area of a moiré unit cell.

IV. QUASIPARTICLES IN FCIS

Now we study quasiparticles for the $\nu_h = 2/3$ moiré FCIs in tMoTe₂. Note that the particle in “quasiparticle” actually means hole here. To generate N_{qp} quasiparticles, we require the number of moiré unit cells N_s and the number of holes N to satisfy $N_s = \frac{1}{2}(3N - N_{\text{qp}})$. It is natural to use a delta impurity potential $U_{\text{imp}}(\mathbf{w})$ of strength U_0 at position \mathbf{w} that is attractive for holes to localize a quasiparticle at \mathbf{w} . The Fourier transform of the impurity potential is $U(\mathbf{q}) = \frac{U_0}{N_s} e^{-i\mathbf{q}\cdot\mathbf{w}}$. In this section, we choose $d = 10$ nm and $\epsilon = 10$, and project the Hamiltonian to the top valence band of the K valley. We will consider other parameter values and include more bands in Appendix C and D.

To reach larger system sizes, we still diagonalize the first two terms (band dispersion and interaction) in Eq. (10) to obtain states of delocalized quasiparticles, for which we have conserved momenta to reduce the many-body Hilbert space dimension. Then we diagonalize the impurity potentials in this subspace of mobile quasiparticles to pin the quasiparticles. Similar to the FQH case, the dimension of the quasiparticle subspace can be predicted by Haldane’s exclusion principle [83]. Naively, this strategy is expected to work well when $\Delta_s \ll U_0 \ll \Delta_g$, such that the the impurity potential can sufficiently mix states within the quasiparticle subspace, but

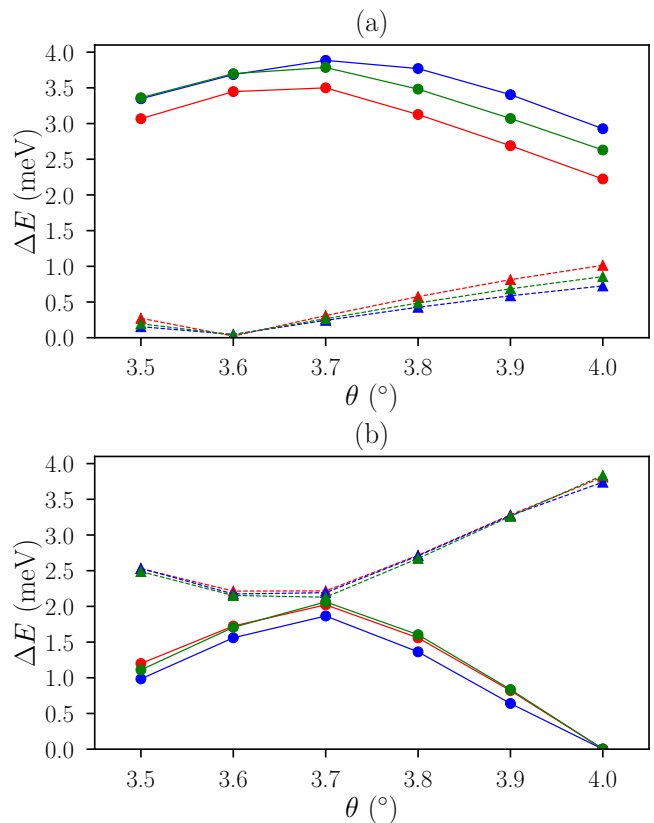


Figure 4. The energy gap (solid lines) and the splitting (dotted lines) of the quasiparticle manifold as a function of the twist angle. We consider the presence of a single delocalized quasiparticle and two delocalized quasiparticles in (a) and (b), respectively. The system sizes are $N = 19, N_s = 28$ (red), $N = 21, N_s = 31$ (blue), $N = 23, N_s = 34$ (green) in (a), and $N = 20, N_s = 29$ (red), $N = 22, N_s = 32$ (blue), $N = 24, N_s = 35$ (green) in (b).

does not couple them to higher levels. Here Δ_g is the energy gap separating the subspace of delocalized quasiparticles from higher excited levels, and Δ_s is the energy splitting within the subspace. However, by diagonalizing the full Hamiltonian Eq. (10) with the single-band projection, we find that the mixing of the quasiparticle subspace with higher excited levels is still very weak even when the strength U_0 of the delta impurity potential has significantly exceeded Δ_g (see Appendix B).

In Fig. 4, we display Δ_g and Δ_s in the presence of one and two delocalized quasiparticles at various twist angles, where Δ_g is defined as the energy difference between the highest level in the quasiparticle subspace and the lowest level out of this subspace. For a single delocalized quasiparticle, we have $\Delta_g > \Delta_s$ in the entire range of $\theta \in [3.5^\circ, 4.0^\circ]$ [Fig. 4(a)]. By contrast, the quasiparticle subspace is significantly broadened when two delocalized quasiparticles are present [Fig. 4(b)]. Moreover, the gap is obviously smaller compared to the single quasiparticle case, reflecting the reduced charge gap in the presence of more quasiparticles. The broadening of the quasiparticle subspace and the shrinking of gap makes $\Delta_s > \Delta_g$ for two delocalized quasiparticles in the entire range of θ con-

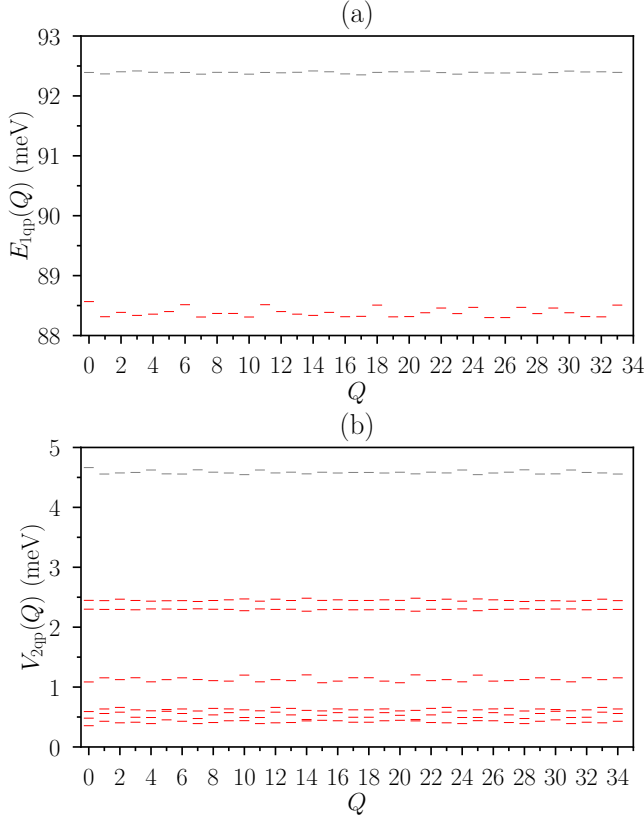


Figure 5. The low-energy energy spectra in presence of (a) a single delocalized quasiparticle and (b) two delocalized quasiparticles. The system sizes are $N = 23, N_s = 34$ in (a) and $N = 24, N_s = 35$ in (b). Q is a proper folding of the two-dimensional momentum \mathbf{Q} . The definitions of E_{1qp} and V_{2qp} are given in the text. The subspace of delocalized quasiparticles are highlighted by red. This subspace contains one level per momentum sector in (a), and six levels per momentum sector in (b). The gray levels are out of this subspace. We set $\theta = 3.7^\circ$, $d = 10$ nm and $\epsilon = 10$.

sidered by us. In this case, the ratio Δ_s/Δ_g is the smallest at $\theta = 3.7^\circ$, which is the minimum (maximum) of Δ_s (Δ_g) [Fig. 4(b)]. We hence fix the twist angle at $\theta = 3.7^\circ$ in the calculations throughout this section.

A. Single delocalized quasiparticles

Using the energy levels in the presence of a single delocalized quasiparticle and the ground energy in the absence of quasiparticles, we can estimate the energy cost of a delocalized quasiparticle excitation. For a system of $N = N_0, N_s = N_{s,0} = 3N_0/2$ without quasiparticles, there are three nearly degenerate FCI ground states with mean energy \bar{E}_{gs} . We define the creation energy of a single delocalized quasiparticle as $E_{1qp}(\mathbf{Q}) \equiv E_{N=N_0+1, N_s=N_{s,0}+1}(\mathbf{Q}) - \bar{E}_{gs}$, where $E_{N=N_0+1, N_s=N_{s,0}+1}(\mathbf{Q})$ is the energy level with momentum \mathbf{Q} of the many-body Hamiltonian H (impurity potential excluded) of the system size $N = N_0 + 1, N_s = N_{s,0} + 1$ (such that one delocalized quasiparticle is added to the ground

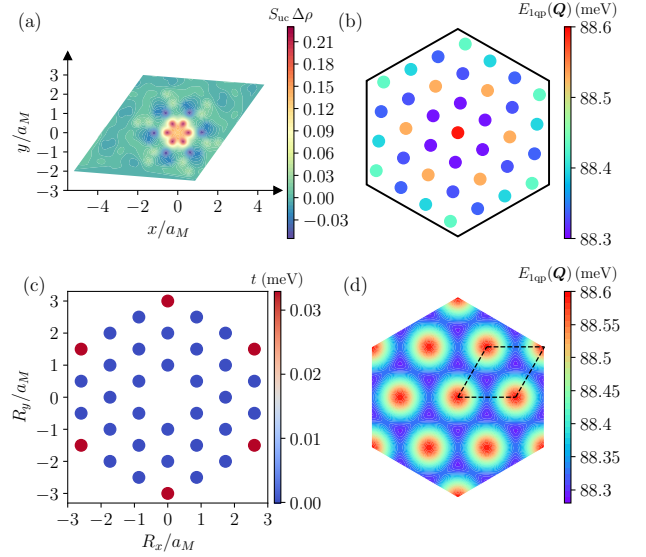


Figure 6. (a) Density distribution of the anyon Wannier state centered at the origin measured relative to the FCI ground state. (b) The single quasiparticle energy $E_{1qp}(\mathbf{Q})$ at discrete momenta \mathbf{Q} . (c) The anyon hopping parameter $t(\mathbf{R})$ between the site at the origin and the site at position \mathbf{R} . (d) Interpolated $E_{1qp}(\mathbf{Q})$ based on Eq. (14). The black dashed lines mark the emergent periodicity in $E_{1qp}(\mathbf{Q})$. The system size is $N = 25$ and $N_s = 37$.

state). We refer to Ref. [89] for the allowed momentum in tilted samples. In our calculations, we do not include the contribution from a uniform neutralizing charge background, which was considered by previous studies of FQH states in Landau levels [91–94]. In Fig. 5(a), we show $E_{1qp}(\mathbf{Q})$ for $N_0 = 22$, whose $\bar{E}_{gs} \approx 1.088$ eV. $E_{1qp}(\mathbf{Q})$ can also be understood as a dispersive band of the single quasiparticle, with Δ_s the bandwidth. This quasiparticle band is quite flat at all twisted angles considered by us.

Analogous to Wannier states in a single-particle Bloch band, anyon Wannier states can be constructed for the single quasiparticle band. Since there is one state per momentum \mathbf{Q} in the single quasiparticle band, there is exactly one anyon Wannier state per unit cell in real space. The valley-polarized FCI state respect the C_{3z} and $C_{2y}\mathcal{T}$ symmetries, where C_{nj} is the n -fold rotation around the j axis and \mathcal{T} is the time reversal symmetry. The symmetry-preserving anyon Wannier states are centered at the \mathcal{R}_M^M sites with positions given by $\mathbf{R} = n_1 \mathbf{a}_1 + n_2 \mathbf{a}_2$, where $n_{1,2}$ are integers.

An anyon Wannier state $|\mathbf{R}\rangle_{1qp}$ centered at \mathbf{R} is a linear superposition of the single quasiparticle states $|\Phi_{\mathbf{Q}}\rangle_{1qp}$ at different momenta \mathbf{Q} ,

$$|\mathbf{R}\rangle_{1qp} = \frac{1}{\sqrt{N_s}} \sum_{j=0}^{N_s-1} e^{i\phi_j} e^{-i\mathbf{Q}_j \cdot \mathbf{R}} |\Phi_{\mathbf{Q}_j}\rangle_{1qp}. \quad (12)$$

For numerically returned states $|\Phi_{\mathbf{Q}}\rangle_{1qp}$ in the subspace of one mobile quasiparticle, we determine the phase factors $e^{i\phi_j}$ as follows. Without loss of generality, we take $\phi_0 = 0$. The remaining phases $\phi_{j \neq 0}$ are fixed by requiring that the matrix

element ${}_{1\text{qp}}\langle\Phi_0|\Delta(\mathbf{r})e^{i\phi_j}|\Phi_{\mathbf{Q}_j}\rangle_{1\text{qp}}$ is real and positive, where $\Delta(\mathbf{r}) = +\sum_{i=1}^N\delta(\mathbf{r}_i)$. This gauge choice maximizes the density at the origin for the Wannier state $|\mathbf{R} = \mathbf{0}\rangle_{1\text{qp}}$ with respect to ϕ_j . A generic Wannier state $|\mathbf{R}' \neq \mathbf{0}\rangle_{1\text{qp}}$ is related to $|\mathbf{R} = \mathbf{0}\rangle_{1\text{qp}}$ by translating all particles by a lattice vector \mathbf{R}' . To illustrate the resulting states, we plot the density difference $\Delta\rho$ between the anyon Wannier state centered at $\mathbf{R} = \mathbf{0}$ and the FCI ground state, as illustrated in Fig. 6(a). As expected, the profile of $\Delta\rho$ is centered at the origin and decays to zero for distance far away from the center. However, $\Delta\rho$ peaks at the six \mathcal{R}_M^X and \mathcal{R}_X^M sites around the origin, following the density distribution in the ground state.

We further calculate the effective anyon hopping parameter $t(\mathbf{R})$ between two \mathcal{R}_M^M sites separated by \mathbf{R} ,

$$t(\mathbf{R}) = {}_{1\text{qp}}\langle\mathbf{R}|H|\mathbf{0}\rangle_{1\text{qp}} = \frac{1}{N_s} \sum_{\mathbf{Q}} e^{i\mathbf{Q}\cdot\mathbf{R}} E_{1\text{qp}}(\mathbf{Q}). \quad (13)$$

$E_{1\text{qp}}(\mathbf{Q})$, the quasiparticle energy measured relative to \bar{E}_{gs} , is plotted in Fig. 6(b) at discrete momenta for the system size $N = 25, N_s = 37$. Based on these values of $E_{1\text{qp}}(\mathbf{Q})$, the calculated $t(\mathbf{R})$ is illustrated in Fig. 6(c). Due to the discrete nature of the Fourier transform in Eq. (13), we obtain 36 independent hopping parameters $t(\mathbf{R} \neq \mathbf{0})$ in addition to the onsite energy $t(\mathbf{0})$ for this system size. An intriguing observation is that the dominant hopping amplitudes occur between sites separated by a distance of three moiré lattice constants. For comparison, $t(|\mathbf{R}| = 3a_M) \approx 0.033$ meV, which is at least two orders of magnitude larger than all other hopping parameters in Fig. 6(c).

Having obtained $t(\mathbf{R})$ using $E_{1\text{qp}}(\mathbf{Q})$ of a finite-size system, we can evaluate $E_{1\text{qp}}(\mathbf{Q})$ in the thermodynamic limit via the inverse Fourier transform

$$E_{1\text{qp}}(\mathbf{Q}) = \sum_{\mathbf{R}} e^{-i\mathbf{Q}\cdot\mathbf{R}} t(\mathbf{R}), \quad (14)$$

where \mathbf{Q} is no longer restricted to the discrete momenta imposed by the finite system size. Fig. 6(d) shows $E_{1\text{qp}}(\mathbf{Q})$ as a function of continuous \mathbf{Q} , which exactly reproduces the discrete values shown in Fig. 6(b). Interestingly, $E_{1\text{qp}}(\mathbf{Q})$ is periodic not only with respect to the moiré Brillouin zone defined by the underlying lattice, but also with respect to a smaller effective Brillouin zone, delineated by the dashed lines in Fig. 6(d). This emergent periodicity arises because $t(\mathbf{R})$ is dominated by hopping between sites separated by $3a_M$, leading to an effective Brillouin zone that is 3×3 smaller than the original one. We note that this emergent periodicity in $E_{1\text{qp}}(\mathbf{Q})$ has recently been independently reported in Ref. [68]. Here we provide a perspective based on the anyon Wannier states and the hopping model.

We compare the interpolated $E_{1\text{qp}}(\mathbf{Q})$ in Fig. 6(d) to the values in Fig. 5(a) at the discrete momenta \mathbf{Q} allowed in a different system size of $N = 23, N_s = 34$. The energy differences at each momentum can be as small as 3×10^{-4} meV and do not exceed 0.026 meV. This close agreement validates the accuracy of the anyon hopping model in capturing the quasiparticle energy dispersion.

B. Two delocalized quasiparticles

Given the nearly flat single-quasiparticle band, the significant broadening of the subspace of two delocalized quasiparticles is a signal of the interaction between quasiparticles. For finite systems it is difficult to precisely subtract the contribution of single-quasiparticle dispersion from the two-quasiparticle spectrum, as their allowed momentum points are different. Here we only make a rough estimation of the interaction between two quasiparticles by calculating $V_{2\text{qp}}(\mathbf{Q}) \equiv E_{N=N_0+2, N_s=N_{s,0}+2}(\mathbf{Q}) - \bar{E}_{\text{gs}} - 2\bar{E}_{1\text{qp}}$, where $E_{N=N_0+2, N_s=N_{s,0}+2}(\mathbf{Q})$ is the energy level with momentum \mathbf{Q} of the many-body Hamiltonian of the system size $N = N_0 + 2, N_s = N_{s,0} + 2$ (such that two delocalized quasiparticles are added to the ground state), and $\bar{E}_{1\text{qp}}$ is the $E_{1\text{qp}}(\mathbf{Q})$ averaged over all momentum sectors. The result for $N_0 = 22$ is displayed in Fig. 5(b), whose $\bar{E}_{1\text{qp}} \approx 0.0884$ eV. Remarkably, $V_{2\text{qp}}$ is positive in all momentum sectors, with the lowest value ≈ 0.35 meV. As the neglected single-quasiparticle bandwidth Δ_s is only ≈ 0.27 meV in this case, it is very likely that the two delocalized quasiparticles have a repulsive interaction.

The interactions between quasiparticles and quasiholes have been studied in the context of Landau levels [95–99]. We do similar analysis for the $\nu = 2/3$ FQH quasiparticles in our LLL setup in Sec. II, using the same system sizes as in Fig. 5. In that case, we also find repulsive interactions between two quasiparticles. A recent work found the crossover from repulsive to attractive interaction between two $\nu = 1/3$ Laughlin quasiholes when the range of the electron-electron interaction is decreased [99]. Our results in both the LLL and tMoTe₂ are consistent with this observation, since the interaction is only weakly screened in our study.

In the following, we include impurity potentials and characterize the localized $\nu_h = 2/3$ FCI quasiparticles in tMoTe₂.

C. Single localized quasiparticle

Let us first consider a single localized quasiparticle of the $\nu_h = 2/3$ FCIs in tMoTe₂. We are interested in the effect of this quasiparticle on particle's real-space density, which is measured by $\Delta\rho(\mathbf{r}) = \rho(\mathbf{r}) - \rho_0(\mathbf{r})$. Here $\rho(\mathbf{r})$ is the particle's density in the presence of a single quasiparticle, and $\rho_0(\mathbf{r})$ is the particle's density in the FCI ground state without quasiparticles [Fig. 3(a)]. In Figs. 7(a), 7(b), and 7(c), we show $\Delta\rho(\mathbf{r})$ for $N = 25, N_s = 37$, which is the largest system size we can reach by ED. The impurity potential is located at \mathcal{R}_M^M , \mathcal{R}_M^X , and the bridge point \mathcal{R}_{Br} (middle of \mathcal{R}_M^X and \mathcal{R}_X^M), respectively. Extra particles indeed concentrate around the impurity potential in all of the three cases, which is a signal of a localized quasiparticle. With increasing distance from the impurity potential, $\Delta\rho(\mathbf{r})$ oscillates and tends to zero. Unlike the FQH case [Fig. 1(a)], the density distribution in the presence of an FCI quasiparticle no longer has continuous rotational symmetry. Moreover, there is a clear dependence of $\Delta\rho(\mathbf{r})$ on the position of the impurity potential. One can see that particles still prefer to occupy \mathcal{R}_M^X and \mathcal{R}_X^M regions as in

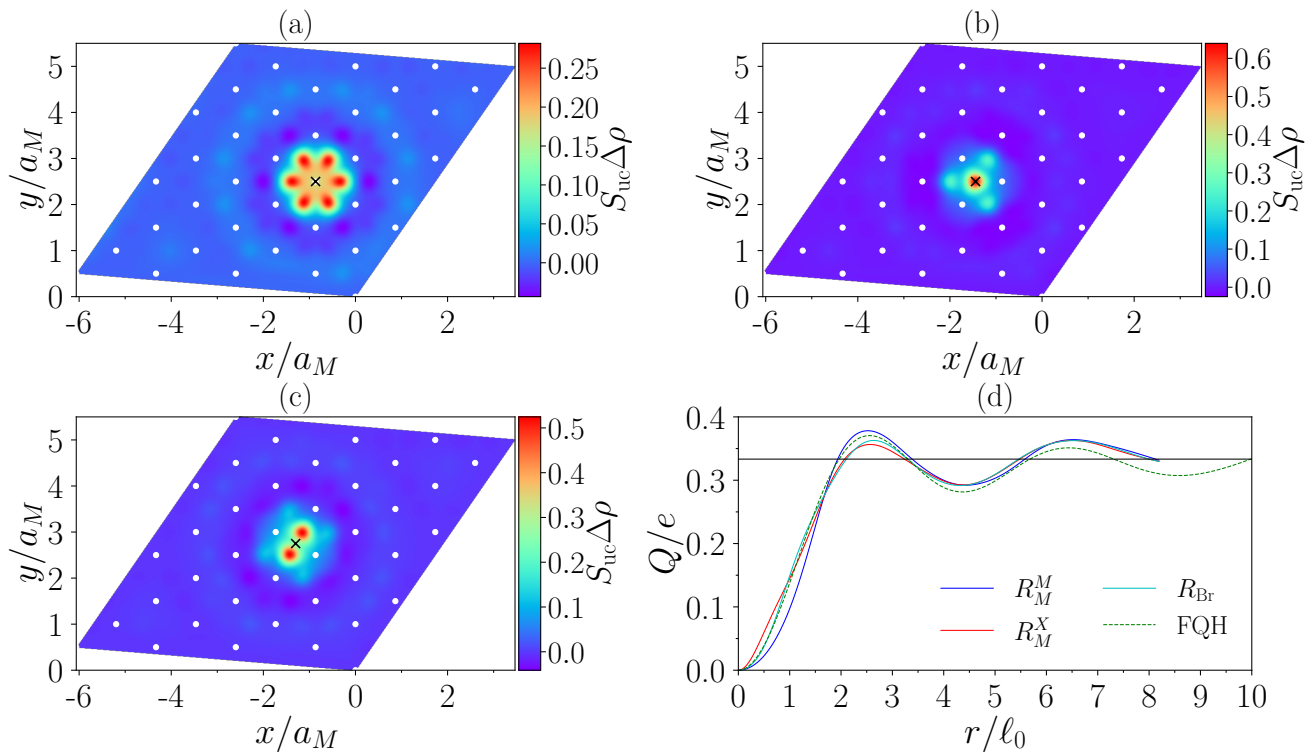


Figure 7. (a)-(c) Density distribution with a single-quasiparticle excitation in the $\nu_h = 2/3$ tMoTe₂ FCI with $N = 25$, $N_s = 37$. The impurity potential (indicated by the black cross) is located at (a) \mathcal{R}_M^M , (b) \mathcal{R}_M^X , and (c) \mathcal{R}_{Br} , respectively. (d) Excess charges corresponding to the three cases in (a)-(c). We also give the data of the $\nu = 2/3$ Coulomb FQH state [dashed line, the same as in Fig. 1(b)] for comparison. The horizontal reference line indicates $Q = e/3$, which is expected for a Laughlin-type quasiparticle.

the ground-state case, such that $\Delta\rho(\mathbf{r})$ demonstrates C_{6z} and C_{3z} rotation symmetry, respectively, if the impurity potential is located at \mathcal{R}_M^M and \mathcal{R}_M^X sites [Figs. 7(a) and 7(b)]. The density profile for the impurity located at \mathcal{R}_M^M closely follows that of the anyon Wannier state shown in Fig. 6(a).

To further characterize the existence of a localized quasiparticle, we compute the charge excess $Q(r)$ as a function of the distance r from the impurity potential, as defined in Eq. (4). Note that in the FCI case both $\rho(\mathbf{r})$ and $\rho_0(\mathbf{r})$ are not uniform or rotationally invariant, and we cannot reduce Eq. (4) to an integral in the radial direction. The results corresponding to Figs. 7(a), 7(b), and 7(c) are similar and we display them in Fig. 7(d). For direct comparison with the FQH data, we choose the effective magnetic length [69]

$$\ell_0 = \left(\frac{\sqrt{3}}{4\pi}\right)^{1/2} a_M \quad (15)$$

as the length unit for tMoTe₂. Under this choice, $d = 10$ nm corresponds to $d/\ell_0 \approx 5$, which is consistent with the setting $d = 5\ell_B$ in Sec. II. When $r \gtrsim 2\ell_0$, one can see oscillations of the excess charge around $e/3$ – the theoretical value of a Laughlin-type quasiparticle. This is a clear signal that the quasiparticle starts nucleating. However, $Q(r)$ does not converge even at the largest r we can reach, suggesting that our system size is still insufficient for the quasiparticle to fully develop. The excess charge of $\nu_h = 2/3$ moiré FCIs is similar to

that of the $\nu = 2/3$ FQH state when the length units are chosen as ℓ_0 and ℓ_B for tMoTe₂ and the LLL, respectively, but the oscillations of $Q(r)$ in the FQH case show quicker damping. If we take the radius of the $\nu = 2/3$ FQH quasiparticle of Coulomb interaction as $6\ell_B$ as suggested by the braiding data in Sec. II C, the $\nu_h = 2/3$ FCI quasiparticle in tMoTe₂ extends within a circle whose radius is at least $6\ell_0 \approx 2.2a_M \approx 120$ Å. This spatial extent could further increase if multiple bands are taken into account, as shown in Appendix D.

D. Braiding of two quasiparticles

We now examine the fractional statistics of quasiparticle excitations in the $\nu_h = 2/3$ tMoTe₂ moiré FCIs. We should emphasize that, while there is no physical magnetic field in moiré FCIs, a real-space Berry curvature $\Omega(\mathbf{r})$ does exist, which contributes to the Berry phase when two localized quasiparticles are braided. This real-space Berry curvature has been reported for tight-binding models [69]. For tMoTe₂, one can demonstrate $\Omega(\mathbf{r})$ by mapping the tMoTe₂ model to a Landau level problem, in which an effective periodic magnetic field with nonzero mean emerges [43]. To numerically probe this real-space Berry curvature, we adiabatically drag a single hole using a mobile impurity potential projected to the top valence band in the K valley. If the hole's wave function accumulates a Berry phase $\Phi(\mathbf{r})$ along a closed path around point

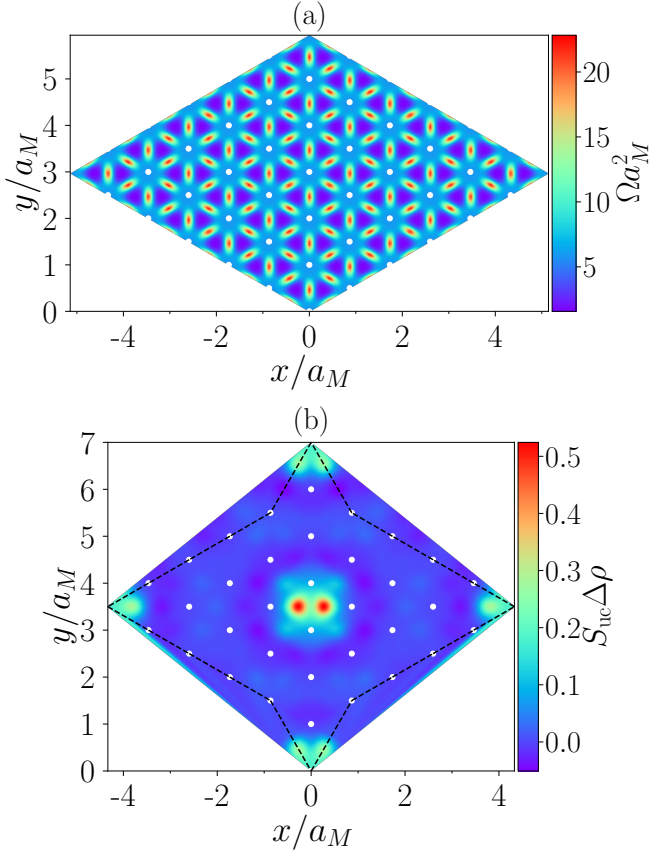


Figure 8. (a) The real-space Berry curvature probed by dragging a hole residing in the K -valley top valence band. (b) Braiding path (dashed line) of two quasiparticles for the system size $N = 24$, $N_s = 35$. The density distribution shown in the plot corresponds to two impurity potentials at the sample center and $\mathbf{r} = (0, 0)$.

\mathbf{r} , we can approximate the real-space Berry curvature at \mathbf{r} as $\Omega(\mathbf{r}) = \lim_{S(\mathbf{r}) \rightarrow 0} \Phi(\mathbf{r})/S(\mathbf{r})$, where $S(\mathbf{r})$ is the area enclosed by the closed path. In Fig. 8(a), we show $\Omega(\mathbf{r})$ for the K -valley top valence band of tMoTe₂ at twist angle $\theta = 3.7^\circ$. It is indeed very similar to the effective magnetic field obtained in Ref. [43]. For a single hole, the accumulated Berry phase along the boundary of a moiré unit cell is 2π . Moreover, dragging a single localized quasiparticle along the same path gives Berry phase $2\pi/3$, which provides another compelling evidence of the fractional charge $e/3$ of the quasiparticle.

Then we fix one impurity potential at the sample center and move the other along a closed path, as shown in Fig. 8(b). We carefully choose the path such that the two impurity potentials are separated as far as possible and the path encloses an integer number of moiré unit cells. The technical method used to extract the Berry phase is the same as that in Sec. II C. The accumulated Berry phase still contains two parts: the AB phase resulting from the real-space Berry curvature $\Omega(\mathbf{r})$, and the anyon statistical phase. The AB phase is just $2\pi/3$ times the number of enclosed moiré unit cells. For the path in Fig. 8(b), we numerically find the anyon statistical phase as 1.311π for $N = 24$, $N_s = 35$, which has reasonably good agreement

with the theoretical prediction $4\pi/3$. Again, the discrepancy is because the quasiparticles are not fully developed and separated in the finite system.

V. TRIAL WAVE FUNCTION FOR ANYONS IN FCIS

We now reveal the connection between the FQH states in the LLL and the FCIs in tMoTe₂ regarding the quasiparticles. The $\nu = 1/3$ Laughlin wave function in the LLL is

$$\Psi_L = \mathcal{N}_L \prod_{1 \leq i < j \leq N} (z_i - z_j)^3 e^{-\frac{1}{4\ell_B^2} \sum_i |z_i|^2}, \quad (16)$$

where $z_j = x_j + iy_j$ is the complex coordinate of particle j , N is the number of particles, and \mathcal{N}_L is a normalization factor. Here we write the wave functions on the disk geometry for symbol simplicity. The quasihole excitation on top of the Laughlin state is given by

$$\Psi_{L,h} = \mathcal{N}_{L,h} \prod_i (z_i - w) \Psi_L, \quad (17)$$

where w is the complex coordinate of the quasihole center and $\mathcal{N}_{L,h}$ is a normalization factor. Both Ψ_L and $\Psi_{L,h}$ are zero-energy eigenstates of the first-order Haldane's pseudopotential interaction [86].

It has been observed that the top moiré valence band of tMoTe₂ is similar to the LLL, as it nearly saturates the trace inequality $T \geq 0$ of the single-particle quantum geometry [39, 43, 100]. Here T is defined as [101–103]

$$T = \min_{\tilde{g}} \left(\frac{1}{2\pi} \int_{\text{MBZ}} \text{tr}_{\tilde{g}} g(\mathbf{k}) \right) - |\mathcal{C}| \quad (18)$$

where $g(\mathbf{k})$ is the quantum metric of the band, and $\text{tr}_{\tilde{g}} g \equiv \sum_{a,b=x,y} \tilde{g}_{ab} g^{ab}$ is the generalized trace with respect to a unimodular matrix \tilde{g} . For the top moiré valence band in tMoTe₂, T is approximately $0.1 \sim 0.3$, as discussed in detail in Appendix D. In comparison, the LLL has exactly $T = 0$ and momentum-independent quantum geometric tensor. More generally, an ideal Chern band with $T = 0$ and momentum-dependent quantum geometries can be viewed as a generalized LLL with the wave functions of the form $\Theta_{\mathbf{k}}(\mathbf{r}) = \mathcal{N}_{\mathbf{k}} \mathcal{B}(\mathbf{r}) \Psi_{0,\mathbf{k}}(\mathbf{r})$, where \mathbf{k} is the wave vector in the Brillouin zone, $\Psi_{0,\mathbf{k}}(\mathbf{r})$ is the magnetic Bloch wave function of the LLL, $\mathcal{B}(\mathbf{r})$ is a \mathbf{k} -independent but spatially-varying function, and $\mathcal{N}_{\mathbf{k}}$ is a normalization factor [79–81]. Since T is small in tMoTe₂, the Bloch wave function $\psi_{\mathbf{k}}(\mathbf{r})$ for its top moiré valence band in K valley can be approximated by $\Theta_{\mathbf{k}}(\mathbf{r})$. We obtain the function $\mathcal{B}(\mathbf{r})$ by maximizing the momentum-averaged value of the overlap $|\langle \psi_{\mathbf{k}} | \Theta_{\mathbf{k}} \rangle|^2$ using a variational approach as outlined in Ref. [82]. The function $\mathcal{B}(\mathbf{r})$ captures the density fluctuations in the moiré band, and $|\mathcal{B}(\mathbf{r})|^2$ peaks at \mathcal{R}_M^X and \mathcal{R}_X^M positions similar to the density shown in Fig. 3(a).

Both the $\nu = 1/3$ Laughlin model wave function in the LLL and its quasihole excitation can be generalized to FCIs in

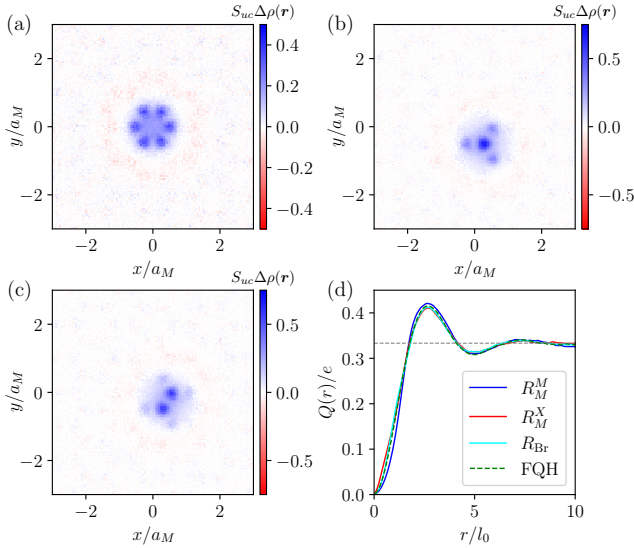


Figure 9. (a)-(c) Monte Carlo results of $\Delta\rho(\mathbf{r})$ using Eq. (19), with a single quasiparticle located at (a) \mathcal{R}_M^M , (b) \mathcal{R}_M^X , and (c) \mathcal{R}_{Br} , respectively. (d) Excess charges corresponding to the three cases in (a)-(c). As a comparison, we plot the excess charge for the LLL using green dashed line (labeled by FQH), which is also obtained using the Monte Carlo simulation. The expected quasiparticle charge $Q = e/3$ is plotted in horizontal dashed line.

a Chern band with the single-particle wave function $\Theta_{\mathbf{k}}(\mathbf{r})$:

$$\begin{aligned}\Phi_L &= \mathcal{N}'_L \prod_i \mathcal{B}(\mathbf{r}_i) \Psi_L, \\ \Phi_{L,h} &= \mathcal{N}'_{L,h} \prod_i (z_i - w) \mathcal{B}(\mathbf{r}_i) \Psi_L,\end{aligned}\quad (19)$$

where \mathcal{N}'_L and $\mathcal{N}'_{L,h}$ are normalization factors. Here Φ_L and $\Phi_{L,h}$ are trial wave functions for, respectively, the FCI ground state and its quasihole excitation at filling $\nu = 1/3$. By performing particle-hole transformation to Φ_L ($\Phi_{L,h}$) within the manifold spanned by $\Theta_{\mathbf{k}}(\mathbf{r})$, we obtain, respectively, the FCI ground state (quasiparticle excitation) at filling $\nu = 2/3$. Therefore, the density distribution $\Delta\rho(\mathbf{r})$ of the FCI quasiparticle at $\nu = 2/3$ can be determined by the density difference between Φ_L and $\Phi_{L,h}$.

With the optimal $\mathcal{B}(\mathbf{r})$ for the K -valley top valence band of tMoTe₂, we separately calculate the density of Φ_L and $\Phi_{L,h}$ using classical Monte Carlo simulation by sampling 3×10^6 configurations (after 10^6 burn-in steps) for a system of $N = 64$ particles, which is far beyond the capability of ED. Figs. 9(a)-9(c) show the Monte Carlo results of $\Delta\rho(\mathbf{r})$ with w located at \mathcal{R}_M^M , \mathcal{R}_M^X , and \mathcal{R}_{Br} , respectively. The quasiparticle density distribution depends on w , capturing all the qualitative features in the ED results shown in Fig. 7. The corresponding excess charges $Q(r)$ of the quasiparticle as functions of distance r from w are shown in Fig. 9(d). Notably, these $Q(r)$ curves, with minor differences at short distances, are all similar with each other, which is consistent with that shown in Fig. 7(d). Based on these comparisons, we conclude that the particle-hole conjugate of $\Phi_{L,h}$ in Eq. (19) provides

a reasonable trial wave function for a localized $\nu_h = 2/3$ FCI quasiparticle in a single top valence band of tMoTe₂ and captures the real-space density distribution. Note that $Q(r)$ obtained from Eq. (19) converges faster to $e/3$ than those in Fig. 7(d), thus $\Phi_{L,h}$ underestimates the spatial extent of the quasiparticle of Coulomb states. In Fig. 7(d), we also plot the Monte Carlo results for $Q(r)$ in the LLL using the wave functions Ψ_L and $\Psi_{L,h}$, which matches quantitatively well with the first-order Haldane's pseudopotential quasiparticle result in Fig. 1(b). Moreover, it is very close to the other three $Q(r)$ curves with nontrivial $\mathcal{B}(\mathbf{r})$. This observation again indicates that the dominant effect of $\mathcal{B}(\mathbf{r})$ is the modulation of charge density only within the scale of a lattice unit cell.

VI. CONCLUSION

In this work, we have investigated the properties of quasiparticles for the $\nu_h = 2/3$ FCI in tMoTe₂ and for the $\nu = 2/3$ FQH state in the LLL. We have proposed a tight-binding model for mobile FCI quasiparticles. We further pin quasiparticles by delta impurity potentials. We get clear signal of the nucleation of localized quasiparticles, as shown by the consistency of numerically obtained charge and braiding phase of quasiparticles with theoretical values. The spatial extent of a localized quasiparticle is also estimated by comparing the accumulated excess charge with the FQH counterpart. Trial wavefunctions of FCI quasiparticles are variationally determined using the nearly ideal quantum geometry of the tMoTe₂ top valence band.

There are several possible future directions based on this work. First, our numerical characterization of FQH/FCI quasiparticles still suffers from non-negligible finite-size effects. Even within the single-band/LLL projection, the localized quasiparticle does not fully develop, as reflected by the oscillating excess charge and residual deviation of the braiding phase from the theoretical value. The $\nu = 2/3$ quasihole is even much bigger, thus we cannot extract useful information about it by ED. We have also made tentative investigations of band mixing effects on FCI quasiparticles in tMoTe₂ (see Appendix D), but the results are limited to smaller systems and much less conclusive. More advanced numerical techniques are hence necessary for solving these problems. If the recent applications of neural-network algorithms to FQH and FCI systems [104–107] can reach larger systems than ED, they might be helpful to characterize the quasiparticle/quasihole more precisely, clarify their response to band mixing in moiré materials, and even study non-Abelian excitations. Second, we only considered the short-range delta impurity potential in this work. It would also be useful to study more realistic long-range impurity potentials, such as the Gaussian potential and the Coulomb potential of a point charge above the sample [85]. Finally, we focused on the anyons of stable $\nu = 2/3$ Laughlin FCIs. As the non-uniform quantum geometry is a distinctive feature of moiré bands compared to Landau levels, it is interesting to systematically study the quantum geometric effect on the interaction between mobile FCI anyons and the spatial structure of localized FCI anyons. For the latter, a

N_s	\mathbf{T}_1	\mathbf{T}_2
14	(4,1)	(2,4)
16	(4,0)	(0,4)
19	(5,2)	(3,5)
28	(6,2)	(1,5)
29	(6,1)	(1,5)
31	(6,1)	(5,6)
32	(6,2)	(2,6)
33	(6,1)	(3,6)
34	(6,1)	(2,6)
35	(6,1)	(1,6)
36	(6,0)	(0,6)
37	(7,3)	(-3,4)

Table I. Sample geometries used in our numerical simulations. The vectors \mathbf{T}_1 and \mathbf{T}_2 give the periodic boundaries of the sample. The two integers (m, n) in the second and the third columns mean $\mathbf{T}_i = m\mathbf{a}_1 + n\mathbf{a}_2$.

density wave halo around anyons is predicted to appear when FCIs compete with charge density waves [108].

ACKNOWLEDGMENTS

We thank Nicolas Regnault and Bo Yang for helpful discussions. This work was supported by the National Natural Science Foundation of China (Grant No. 12374149, 12350403, and 12274333). F. W. is also supported National Key Research and Development Program of China (Grants No. 2021YFA1401300 and No. 2022YFA1402400). Part of the numerical calculations in this paper have been done on the supercomputing system in the Supercomputing Center of Wuhan University.

Appendix A: Tilted sample

In the system sizes tractable by ED, we often use the tilted geometry to make the sample to be as isotropic as possible. This is necessary for developing localized quasiparticles. The periodic boundary conditions of tilted samples are determined by two vectors \mathbf{T}_1 and \mathbf{T}_2 , which are in general the integer superpositions of both \mathbf{a}_1 and \mathbf{a}_2 . If \mathbf{T}_i is simply proportional to \mathbf{a}_i in both directions, we return to regular samples. In Table I, we summarize the sample geometries used in this work.

Appendix B: Diagonalize the full Hamiltonian of tMoTe₂

In Sec. IV of the main text, we first target on translational invariant tMoTe₂ systems with extra holes and moiré unit cells to get the subspace of delocalized quasiparticles, then diagonalize the impurity potentials to get the states with localized quasiparticles. Now we use an alternative method: we directly diagonalize the full Hamiltonian, including the band dispersion, interactions, and impurity potentials. Single-band

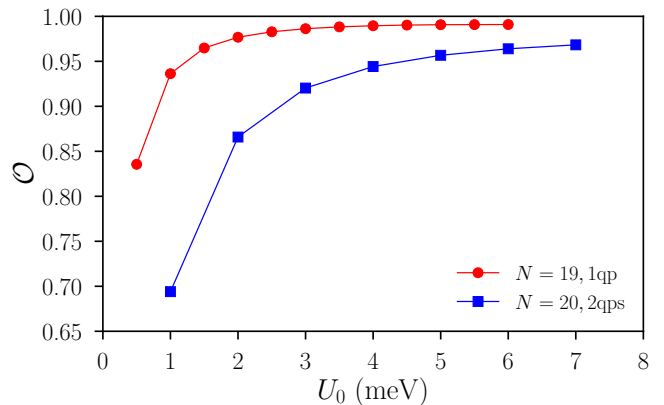


Figure 10. The overlap between the ground states obtained by diagonalizing the full tMoTe₂ Hamiltonian and those obtained by diagonalizing the impurity potential in the quasiparticle subspace. We consider two system sizes: $N = 19, N_s = 28$ and $N = 20, N_s = 29$, corresponding to the presence of one and two localized quasiparticles, respectively. The single quasiparticle is pinned at the sample center. The two quasiparticles are located at the sample center and $\mathbf{r} = (0, 0)$. Single-band projection to the top valence band of K valley is used.

projection in the K valley is still imposed, and model parameters are the same as those in Sec. IV. As the momentum is no longer a good quantum number when diagonalizing the full Hamiltonian, our calculations are limited to smaller system sizes than in Sec. IV.

In Fig. 10, we compare the ground states obtained by this alternative method with those in Sec. IV for one and two localized quasiparticles. With the increasing of impurity potential strength U_0 , the overlap grows quickly. For the single-quasiparticle case, the overlap has reached $\approx 94\%$ when $U_0 = 1$ meV. However, $U_0 = 4$ meV is needed for the two-quasiparticle case if we want to reach the same high overlap, probably because the two quasiparticles are not well separated from each other in the finite system.

We hence estimate the impurity potential strength required to pin an isolate $\nu_h = 2/3$ FCI quasiparticle as ~ 1 meV. This strength is still much smaller than the band gap of the top valence band in the single valley, which is ≈ 8.6 meV. In particular, we also notice that the overlaps are still growing even when U_0 has exceeded the gap separating the quasiparticle subspace and higher excited levels (Fig. 4), indicating that the quasiparticle states cannot be mixed with other states by strong delta impurities. This also happens for the $\nu = 1/3$ model Laughlin quasiholes, which are always the zero-energy ground states of the first-order Haldane pseudopotential combined with the delta pinning potential irrespective of the potential strength.

Appendix C: Dependence on dielectric constant

In Sec. IV of the main text, we fix the dielectric constant as $\epsilon = 10$. We have tried another value $\epsilon = 15$. In Fig. 11,

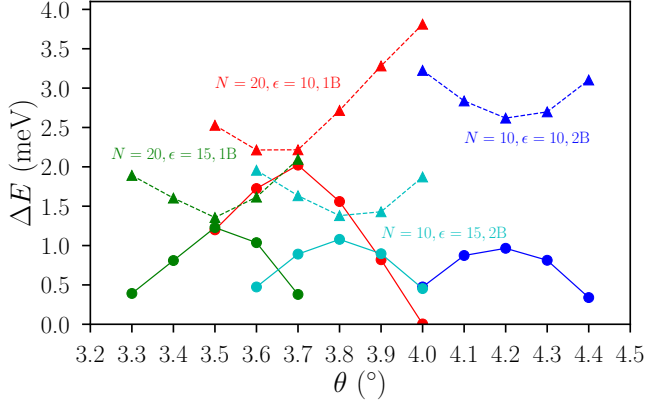


Figure 11. The energy gap (solid lines) and the splitting (dotted lines) of the two-quasiparticle manifold in tMoTe₂ as a function of the twist angle. “1B” means the projection to the top valence band in the K valley, and “2B” means the projection to the top and the second valence bands in the K valley. The system size and the dielectric constant are given in the texts near the corresponding data points. We do not restrict hole’s occupation in the second valence band here.

we repeat the calculations of Fig. 4(b) with this new parameter. Within single-band projection, we find the optimal twist angle, corresponding to the narrowest subspace of two delocalized quasiparticles, moves to $\theta = 3.5^\circ$. The real-space density distribution around a single localized quasiparticle is very similar to that for $\theta = 3.7^\circ$, $\epsilon = 10$ (not shown here).

Appendix D: Two-band simulations

In Sec. IV of the main text, we project the Hamiltonian to the K -valley top valence band only. For the model parameters chosen by us, we have checked that the delocalized quasiparticle subspace in the presence of either a single or two quasiparticles is still valley polarized if we keep the top valence bands in both valleys.

In this section, to further explore the multi-band effects on FCI quasiparticles, we stick with the valley polarization, but keep the top and the second valence bands in the K valley. The Hilbert space significantly grows when two bands are kept, so we can only reach much smaller systems compared with the single-band case. However, we still make efforts to study samples as large as possible by employing the “band maximum” technique introduced in Ref. [47]. This method limits the number of holes occupying the second valence band while leaving the occupation in the top valence band unrestricted. We will gradually increase N_{b2} , the number of holes in the second valence band, to include the band mixing in a controlled way. The single-band projection is recovered when $N_{b2} = 0$. For small N_{b2} , the Hilbert space dimension is reduced a lot compared with the case of unrestricted hole occupation in the second valence band, so that the corresponding system sizes may become tractable for ED. Further reduction of the Hilbert space dimension can be realized by forbidding hole’s occupation in specific momentum points, but we do not

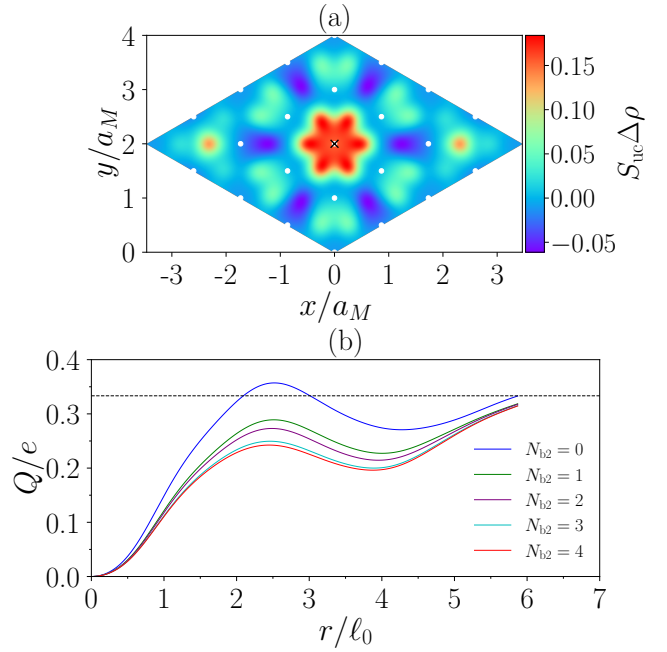


Figure 12. (a) Density profile around a single quasiparticle excitation in the $\nu_h = 2/3$ tMoTe₂ FCI with $N = 11$, $N_s = 16$. We set $N_{b2} = N$, so hole’s occupation in the second valence band is unrestricted. The impurity potential (indicated by the black cross) is located at R_M^M . (b) Excess charge in the presence of a single-quasiparticle excitation in the $\nu_h = 2/3$ tMoTe₂ FCI with $N = 13$, $N_s = 19$. Here we compare the data obtained with different N_{b2} . The horizontal line indicates $Q = e/3$, which is expected for a Laughlin-type quasiparticle.

implement that in our work.

Like in the main text, we will first obtain the quasiparticle subspace under two-band projection with a specific N_{b2} , then diagonalize the impurity potential within this subspace to localize the quasiparticles. In Fig. 11, we display the energy gap and splitting of the quasiparticle subspace in the presence of two delocalized quasiparticles for $N = 10$, $N_s = 14$. In this case we allow all holes occupying the second valence band, i.e., $N_{b2} = N$. The optimal twist angle corresponding to the smallest spreading is 4.2° and 3.8° for $\epsilon = 10$ and $\epsilon = 15$, respectively. In both cases we obtain similar results. We will focus on $\epsilon = 15$, $\theta = 3.8^\circ$ in what follows.

In Fig. 12(a), we display the profile of a single quasiparticle for $N = 11$, $N_s = 16$, $N_{b2} = N$, with the impurity potential located at the R_M^M point. This is the largest system we can reach under two-band projection if the hole’s occupation in the second valence band is unrestricted. Clearly the quasiparticle is not well developed for this system size. Compared with Fig. 7, the density discrepancy still strongly oscillates in the entire sample. In Fig. 12(b), we gradually increase N_{b2} in a larger system size $N = 11$, $N_s = 19$ to demonstrate how the localized quasiparticle is affected by the band mixing. In the limit of $N_{b2} = 0$, the excess charge as a function of distance r from the impurity potential is very similar to that shown in Fig. 7(d). With the increasing of N_{b2} , the first peak of $Q(r)$ is gradually suppressed, such that $Q(r)$ does not oscillate around

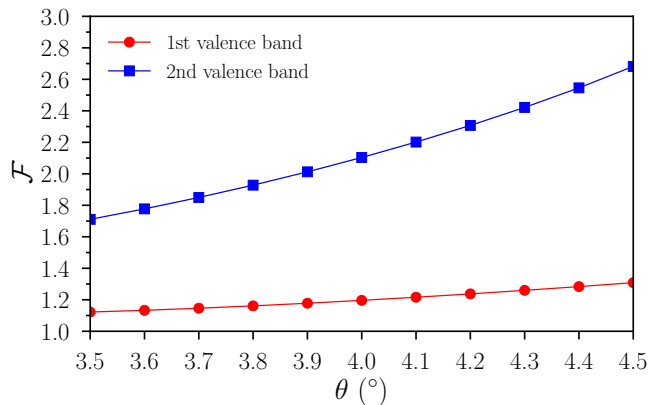


Figure 13. The quantity \mathcal{F} defined in Eq. (D1) as a function of twist angle θ for the top and the second valence bands of tMoTe₂ in the K valley.

$e/3$ at the available values of r . We notice that the curve does not change much from $N_{b2} = 3$ to $N_{b2} = 4$, so probably $N_{b2} = 4$ is already close to the case of $N_{b2} = N$.

The appreciable suppression of the first peak of $Q(r)$ was also observed using the delta impurity potential for the $\nu = 1/3$ Laughlin state of electrons in the second Landau level [85]. So it may be useful to compare the top and the second tMoTe₂ valence bands with conventional Landau levels. In the aspect of single-particle quantum geometry, a convenient indicator of their similarity is

$$\mathcal{F} \equiv \min_{\tilde{g}} \left(\frac{1}{2\pi} \int_{\text{MBZ}} \text{tr}_{\tilde{g}} g(\mathbf{k}) \right), \quad (\text{D1})$$

where $g(\mathbf{k})$ is the quantum metric of a specific band. For the LLL and the second Landau level, \mathcal{F} takes the value of 1 and 3, respectively. In Fig. 13, we show \mathcal{F} for the top and the second valence bands of tMoTe₂ as a function of $\theta \in [3.0^\circ, 4.5^\circ]$. In the entire range of θ , we find for both bands that the minimum in Eq. (D1) is always reached when \tilde{g} is a 2×2 identity matrix. For the top valence band, \mathcal{F} only grows from 1.1 to 1.3 with increasing θ , suggesting the geometric similarity with the LLL. By contrast, \mathcal{F} of the second valence band grows more quickly from 1.7 to 2.7 with increasing θ , which implies that the second valence band might be a superposition of the lowest and the second LLs [103]. Therefore, the band mixing in tMoTe₂ could be analogous to the mixing of the LLL and the second Landau level.

It requires more advanced numerical simulations in sufficiently large systems to conclude whether the suppression of the first peak of $Q(r)$ in the presence of band mixing is a finite-size effect, or a signal of larger spatial extension of the quasiparticle. Ref. [85] found that long-range impurity potentials (like the Gaussian potential, or the Coulomb potential of a point charge above the sample) perform better than the delta potential to localize a $\nu = 1/3$ Laughlin quasihole in the second Landau level, but even in that case the obtained spatial extension of the quasihole is 1.75 times larger than that in the LLL. Since the second valence band of tMoTe₂ may have significant weight on the second Landau level, the band mixing in tMoTe₂ could also increase the size of the $\nu_h = 2/3$ FCI quasiparticle.

-
- [1] D. C. Tsui, H. L. Stormer, and A. C. Gossard, Two-dimensional magnetotransport in the extreme quantum limit, *Phys. Rev. Lett.* **48**, 1559 (1982).
 - [2] R. B. Laughlin, Anomalous quantum hall effect: An incompressible quantum fluid with fractionally charged excitations, *Phys. Rev. Lett.* **50**, 1395 (1983).
 - [3] K. Sun, Z. Gu, H. Katsura, and S. Das Sarma, Nearly flatbands with nontrivial topology, *Phys. Rev. Lett.* **106**, 236803 (2011).
 - [4] E. Tang, J.-W. Mei, and X.-G. Wen, High-temperature fractional quantum hall states, *Phys. Rev. Lett.* **106**, 236802 (2011).
 - [5] T. Neupert, L. Santos, C. Chamon, and C. Mudry, Fractional quantum hall states at zero magnetic field, *Phys. Rev. Lett.* **106**, 236804 (2011).
 - [6] D. N. Sheng, Z.-C. Gu, K. Sun, and L. Sheng, Fractional quantum Hall effect in the absence of Landau levels, *Nature Commun.* **2**, 389 (2011).
 - [7] N. Regnault and B. A. Bernevig, Fractional chern insulator, *Phys. Rev. X* **1**, 021014 (2011).
 - [8] S. A. Parameswaran, R. Roy, and S. L. Sondhi, Fractional quantum hall physics in topological flat bands, *Comptes Rendus Physique* **14**, 816 (2013).
 - [9] E. J. Bergholtz and Z. Liu, Topological flat band models and fractional chern insulators, *Int. J. Mod. Phys. B* **27**, 1330017 (2013).
 - [10] Z. Liu and E. J. Bergholtz, Recent developments in fractional chern insulators, in *Encyclopedia of Condensed Matter Physics (Second Edition)*, edited by T. Chakraborty (Academic Press, Oxford, 2024) second edition ed., pp. 515–538.
 - [11] A. Abouelkomsan, Z. Liu, and E. J. Bergholtz, Particle-hole duality, emergent fermi liquids, and fractional chern insulators in moiré flatbands, *Phys. Rev. Lett.* **124**, 106803 (2020).
 - [12] C. Repellin and T. Senthil, Chern bands of twisted bilayer graphene: Fractional Chern insulators and spin phase transition, *Physical Review Research* **2**, 023238 (2020).
 - [13] P. J. Ledwith, G. Tarnopolsky, E. Khalaf, and A. Vishwanath, Fractional chern insulator states in twisted bilayer graphene: An analytical approach, *Phys. Rev. Research* **2**, 023237 (2020).
 - [14] Z. Liu, A. Abouelkomsan, and E. J. Bergholtz, Gate-tunable fractional chern insulators in twisted double bilayer graphene, *Phys. Rev. Lett.* **126**, 026801 (2021).
 - [15] H. Li, U. Kumar, K. Sun, and S.-Z. Lin, Spontaneous fractional chern insulators in transition metal dichalcogenide moiré superlattices, *Phys. Rev. Res.* **3**, L032070 (2021).
 - [16] V. Crépel and L. Fu, Anomalous hall metal and fractional chern insulator in twisted transition metal dichalcogenides, *Phys. Rev. B* **107**, L201109 (2023).
 - [17] Y. Wang, J. Choe, E. Anderson, W. Li, J. Ingham, E. A. Arsenault, Y. Li, X. Hu, T. Taniguchi, K. Watanabe, X. Roy,

- D. Basov, D. Xiao, R. Queiroz, J. C. Hone, X. Xu, and X. Y. Zhu, Hidden states and dynamics of fractional fillings in twisted mote2 bilayers, *Nature* **641**, 1149 (2025).
- [18] Y. Xie, A. T. Pierce, J. M. Park, D. E. Parker, E. Khalaf, P. Ledwith, Y. Cao, S. H. Lee, S. Chen, P. R. Forrester, *et al.*, Fractional chern insulators in magic-angle twisted bilayer graphene, *Nature* **600**, 439 (2021).
- [19] Z. Lu, T. Han, Y. Yao, A. P. Reddy, J. Yang, J. Seo, K. Watanabe, T. Taniguchi, L. Fu, and L. Ju, Fractional quantum anomalous hall effect in multilayer graphene, *Nature* **626**, 759 (2024).
- [20] J. Xie, Z. Huo, X. Lu, Z. Feng, Z. Zhang, W. Wang, Q. Yang, K. Watanabe, T. Taniguchi, K. Liu, Z. Song, X. C. Xie, J. Liu, and X. Lu, Tunable fractional chern insulators in rhombohedral graphene superlattices, *Nature Materials* **10.1038/s41563-025-02225-7** (2025).
- [21] Z. Lu, T. Han, Y. Yao, Z. Hadjri, J. Yang, J. Seo, L. Shi, S. Ye, K. Watanabe, T. Taniguchi, and L. Ju, Extended quantum anomalous hall states in graphene/hbn moiré superlattices, *Nature* **637**, 1090 (2025).
- [22] S. H. Aronson, T. Han, Z. Lu, Y. Yao, K. Watanabe, T. Taniguchi, L. Ju, and R. C. Ashoori, Displacement field-controlled fractional chern insulators and charge density waves in a graphene/hbn moiré superlattice (2024), [arXiv:2408.11220 \[cond-mat.mes-hall\]](https://arxiv.org/abs/2408.11220).
- [23] J. Xie, Z. Huo, X. Lu, Z. Feng, Z. Zhang, W. Wang, Q. Yang, K. Watanabe, T. Taniguchi, K. Liu, Z. Song, X. C. Xie, J. Liu, and X. Lu, Tunable fractional chern insulators in rhombohedral graphene superlattices (2025), [arXiv:2405.16944 \[cond-mat.mes-hall\]](https://arxiv.org/abs/2405.16944).
- [24] H. Park, J. Cai, E. Anderson, Y. Zhang, J. Zhu, X. Liu, C. Wang, W. Holtzmann, C. Hu, Z. Liu, T. Taniguchi, K. Watanabe, J.-H. Chu, T. Cao, L. Fu, W. Yao, C.-Z. Chang, D. Cobden, D. Xiao, and X. Xu, Observation of fractionally quantized anomalous hall effect, *Nature* **622**, 74 (2023).
- [25] Y. Zeng, Z. Xia, K. Kang, J. Zhu, P. Knüppel, C. Vaswani, K. Watanabe, T. Taniguchi, K. F. Mak, and J. Shan, Thermodynamic evidence of fractional chern insulator in moiré mote2, *Nature* **622**, 69 (2023).
- [26] J. Cai, E. Anderson, C. Wang, X. Zhang, X. Liu, W. Holtzmann, Y. Zhang, F. Fan, T. Taniguchi, K. Watanabe, Y. Ran, T. Cao, L. Fu, D. Xiao, W. Yao, and X. Xu, Signatures of fractional quantum anomalous hall states in twisted mote2, *Nature* **622**, 63 (2023).
- [27] F. Xu, Z. Sun, T. Jia, C. Liu, C. Xu, C. Li, Y. Gu, K. Watanabe, T. Taniguchi, B. Tong, J. Jia, Z. Shi, S. Jiang, Y. Zhang, X. Liu, and T. Li, Observation of integer and fractional quantum anomalous hall effects in twisted bilayer mote2, *Phys. Rev. X* **13**, 031037 (2023).
- [28] Z. Ji, H. Park, M. E. Barber, C. Hu, K. Watanabe, T. Taniguchi, J.-H. Chu, X. Xu, and Z.-X. Shen, Local probe of bulk and edge states in a fractional chern insulator, *Nature* **635**, 578 (2024).
- [29] E. Redekop, C. Zhang, H. Park, J. Cai, E. Anderson, O. Sheekey, T. Arp, G. Babikyan, S. Salters, K. Watanabe, T. Taniguchi, M. E. Huber, X. Xu, and A. F. Young, Direct magnetic imaging of fractional chern insulators in twisted mote2, *Nature* **635**, 584 (2024).
- [30] H. Park, W. Li, C. Hu, C. Beach, M. Gonçalves, J. F. Mendez-Valderrama, J. Herzog-Arbeitman, T. Taniguchi, K. Watanabe, D. Cobden, L. Fu, B. A. Bernevig, N. Regnault, J.-H. Chu, D. Xiao, and X. Xu, Observation of high-temperature dissipationless fractional chern insulator (2025), [arXiv:2503.10989 \[cond-mat.mes-hall\]](https://arxiv.org/abs/2503.10989).
- [31] F. Xu, Z. Sun, J. Li, C. Zheng, C. Xu, J. Gao, T. Jia, K. Watanabe, T. Taniguchi, B. Tong, L. Lu, J. Jia, Z. Shi, S. Jiang, Y. Zhang, Y. Zhang, S. Lei, X. Liu, and T. Li, Signatures of unconventional superconductivity near reentrant and fractional quantum anomalous hall insulators (2025), [arXiv:2504.06972 \[cond-mat.mes-hall\]](https://arxiv.org/abs/2504.06972).
- [32] Z. Dong, A. S. Patri, and T. Senthil, Theory of quantum anomalous hall phases in pentalayer rhombohedral graphene moiré structures, *Phys. Rev. Lett.* **133**, 206502 (2024).
- [33] B. Zhou, H. Yang, and Y.-H. Zhang, Fractional quantum anomalous hall effects in rhombohedral multilayer graphene in the moiréless limit and in coulomb imprinted superlattice (2023), [arXiv:2311.04217 \[cond-mat.str-el\]](https://arxiv.org/abs/2311.04217).
- [34] J. Dong, T. Wang, T. Wang, T. Soejima, M. P. Zaletel, A. Vishwanath, and D. E. Parker, Anomalous hall crystals in rhombohedral multilayer graphene. i. interaction-driven chern bands and fractional quantum hall states at zero magnetic field, *Phys. Rev. Lett.* **133**, 206503 (2024).
- [35] T. Soejima, J. Dong, T. Wang, T. Wang, M. P. Zaletel, A. Vishwanath, and D. E. Parker, Anomalous hall crystals in rhombohedral multilayer graphene ii: General mechanism and a minimal model (2024), [arXiv:2403.05522 \[cond-mat.str-el\]](https://arxiv.org/abs/2403.05522).
- [36] Z. Guo, X. Lu, B. Xie, and J. Liu, Fractional chern insulator states in multilayer graphene moiré superlattices, *Phys. Rev. B* **110**, 075109 (2024).
- [37] C. Wang, X.-W. Zhang, X. Liu, Y. He, X. Xu, Y. Ran, T. Cao, and D. Xiao, Fractional chern insulator in twisted bilayer mote2, *Phys. Rev. Lett.* **132**, 036501 (2024).
- [38] A. P. Reddy, F. Alsallom, Y. Zhang, T. Devakul, and L. Fu, Fractional quantum anomalous hall states in twisted bilayer mote2 and wse2, *Phys. Rev. B* **108**, 085117 (2023).
- [39] N. Morales-Durán, J. Wang, G. R. Schleder, M. Angeli, Z. Zhu, E. Kaxiras, C. Repellin, and J. Cano, Pressure-enhanced fractional chern insulators along a magic line in moiré transition metal dichalcogenides, *Phys. Rev. Res.* **5**, L032022 (2023).
- [40] J. Yu, J. Herzog-Arbeitman, M. Wang, O. Vafek, B. A. Bernevig, and N. Regnault, Fractional chern insulators versus nonmagnetic states in twisted bilayer mote2, *Phys. Rev. B* **109**, 045147 (2024).
- [41] A. Abouelkomsan, A. P. Reddy, L. Fu, and E. J. Bergholtz, Band mixing in the quantum anomalous hall regime of twisted semiconductor bilayers, *Phys. Rev. B* **109**, L121107 (2024).
- [42] C. Xu, J. Li, Y. Xu, Z. Bi, and Y. Zhang, Maximally localized wannier functions, interaction models, and fractional quantum anomalous hall effect in twisted bilayer mote2, *Proceedings of the National Academy of Sciences* **121**, e2316749121 (2024), <https://www.pnas.org/doi/pdf/10.1073/pnas.2316749121>.
- [43] N. Morales-Durán, N. Wei, J. Shi, and A. H. MacDonald, Magic angles and fractional chern insulators in twisted homobilayer transition metal dichalcogenides, *Phys. Rev. Lett.* **132**, 096602 (2024).
- [44] Y. Jia, J. Yu, J. Liu, J. Herzog-Arbeitman, Z. Qi, H. Pi, N. Regnault, H. Weng, B. A. Bernevig, and Q. Wu, Moiré fractional chern insulators. i. first-principles calculations and continuum models of twisted bilayer mote2, *Phys. Rev. B* **109**, 205121 (2024).
- [45] J. Herzog-Arbeitman, Y. Wang, J. Liu, P. M. Tam, Z. Qi, Y. Jia, D. K. Efetov, O. Vafek, N. Regnault, H. Weng, Q. Wu, B. A. Bernevig, and J. Yu, Moiré fractional chern insulators. ii. first-principles calculations and continuum models of rhombohedral graphene superlattices, *Phys. Rev. B* **109**, 205122 (2024).
- [46] Y. H. Kwan, J. Yu, J. Herzog-Arbeitman, D. K. Efetov, N. Regnault, and B. A. Bernevig, Moiré fractional chern insulators

- iii: Hartree-fock phase diagram, magic angle regime for chern insulator states, the role of the moiré potential and goldstone gaps in rhombohedral graphene superlattices (2023), [arXiv:2312.11617](https://arxiv.org/abs/2312.11617) [cond-mat.str-el].
- [47] J. Yu, J. Herzog-Arbeitman, Y. H. Kwan, N. Regnault, and B. A. Bernevig, Moiré fractional chern insulators iv: Fluctuation-driven collapse of fcis in multi-band exact diagonalization calculations on rhombohedral graphene (2024), [arXiv:2407.13770](https://arxiv.org/abs/2407.13770) [cond-mat.str-el].
- [48] H. Li, B. A. Bernevig, and N. Regnault, Multi-band exact diagonalization and an iteration approach to hunt for fractional chern insulators in rhombohedral multilayer graphene (2025), [arXiv:2504.20140](https://arxiv.org/abs/2504.20140) [cond-mat.str-el].
- [49] P. A. Nosov, Z. Han, and E. Khalaf, Anyon superconductivity and plateau transitions in doped fractional quantum anomalous hall insulators (2025), [arXiv:2506.02108](https://arxiv.org/abs/2506.02108) [cond-mat.str-el].
- [50] Z. D. Shi and T. Senthil, Anyon delocalization transitions out of a disordered fqah insulator (2025), [arXiv:2506.02128](https://arxiv.org/abs/2506.02128) [cond-mat.str-el].
- [51] X. G. WEN, Topological orders in rigid states, *International Journal of Modern Physics B* **04**, 239 (1990), <https://doi.org/10.1142/S0217979290000139>.
- [52] X. G. Wen and Q. Niu, Ground-state degeneracy of the fractional quantum hall states in the presence of a random potential and on high-genus riemann surfaces, *Phys. Rev. B* **41**, 9377 (1990).
- [53] G. Moore and N. Read, Nonabelions in the fractional quantum hall effect, *Nuclear Physics B* **360**, 362 (1991).
- [54] D. E. Feldman and B. I. Halperin, Fractional charge and fractional statistics in the quantum hall effects, *Reports on Progress in Physics* **84**, 076501 (2021).
- [55] C. de C. Chamon, D. E. Freed, S. A. Kivelson, S. L. Sondhi, and X. G. Wen, Two point-contact interferometer for quantum hall systems, *Phys. Rev. B* **55**, 2331 (1997).
- [56] S. Das Sarma, M. Freedman, and C. Nayak, Topologically protected qubits from a possible non-abelian fractional quantum hall state, *Phys. Rev. Lett.* **94**, 166802 (2005).
- [57] A. Stern and B. I. Halperin, Proposed experiments to probe the non-abelian $\nu = 5/2$ quantum hall state, *Phys. Rev. Lett.* **96**, 016802 (2006).
- [58] P. Bonderson, A. Kitaev, and K. Shtengel, Detecting non-abelian statistics in the $\nu = 5/2$ fractional quantum hall state, *Phys. Rev. Lett.* **96**, 016803 (2006).
- [59] R. L. Willett, L. N. Pfeiffer, and K. W. West, Measurement of filling factor $5/2$ quasiparticle interference with observation of charge $e/4$ and $e/2$ period oscillations, *Proceedings of the National Academy of Sciences* **106**, 8853 (2009), <https://www.pnas.org/doi/pdf/10.1073/pnas.0812599106>.
- [60] B. I. Halperin, A. Stern, I. Neder, and B. Rosenow, Theory of the fabry-pérot quantum hall interferometer, *Phys. Rev. B* **83**, 155440 (2011).
- [61] B. Rosenow and S. H. Simon, Telegraph noise and the fabry-perot quantum hall interferometer, *Phys. Rev. B* **85**, 201302 (2012).
- [62] J. Nakamura, S. Liang, G. C. Gardner, and M. J. Manfra, Direct observation of anyonic braiding statistics, *Nature Physics* **16**, 931 (2020).
- [63] B. Ghosh, M. Labendik, V. Umansky, M. Heiblum, and D. F. Mross, Coherent bunching of anyons and dissociation in an interference experiment, *Nature* **10.1038/s41586-025-09143-3** (2025).
- [64] H. Bartolomei, M. Kumar, R. Bisognin, A. Marguerite, J.-M. Berroir, E. Bocquillon, B. Plaçais, A. Cavanna, Q. Dong, U. Gennser, Y. Jin, and G. Fève, Fractional statistics in anyon collisions, *Science* **368**, 173 (2020), <https://www.science.org/doi/pdf/10.1126/science.aaz5601>.
- [65] J.-Y. M. Lee and H. S. Sim, Non-abelian anyon collider, *Nature Communications* **13**, 6660 (2022).
- [66] Z. Papić, R. S. K. Mong, A. Yazdani, and M. P. Zaletel, Imaging anyons with scanning tunneling microscopy, *Phys. Rev. X* **8**, 011037 (2018).
- [67] J. S. Douglas and K. Burnett, Imaging of quantum hall states in ultracold atomic gases, *Phys. Rev. A* **84**, 053608 (2011).
- [68] M. Gonçalves, J. F. Mendez-Valderrama, J. Herzog-Arbeitman, J. Yu, X. Xu, D. Xiao, B. A. Bernevig, and N. Regnault, Spinless and spinful charge excitations in moiré fractional chern insulators (2025), [arXiv:2506.05330](https://arxiv.org/abs/2506.05330) [cond-mat.str-el].
- [69] Z. Liu, R. N. Bhatt, and N. Regnault, Characterization of quasiholes in fractional chern insulators, *Phys. Rev. B* **91**, 045126 (2015).
- [70] I. D. Rodríguez and A. E. B. Nielsen, Continuum limit of lattice models with Laughlin-like ground states containing quasiholes, *Phys. Rev. B* **92**, 125105 (2015).
- [71] A. E. B. Nielsen, I. Glasser, and I. D. Rodríguez, Quasielectrons as inverse quasiholes in lattice fractional quantum hall models, *New Journal of Physics* **20**, 033029 (2018).
- [72] M. Račiūnas, F. N. Únal, E. Anisimovas, and A. Eckardt, Creating, probing, and manipulating fractionally charged excitations of fractional chern insulators in optical lattices, *Phys. Rev. A* **98**, 063621 (2018).
- [73] R. O. Umucal ılar, Real-space probe for lattice quasiholes, *Phys. Rev. A* **98**, 063629 (2018).
- [74] B. d. z. Jaworowski, N. Regnault, and Z. Liu, Characterization of quasiholes in two-component fractional quantum hall states and fractional chern insulators in $|c|=2$ flat bands, *Phys. Rev. B* **99**, 045136 (2019).
- [75] E. Macaluso, T. Comparin, R. O. Umucal ılar, M. Gerster, S. Montangero, M. Rizzi, and I. Carusotto, Charge and statistics of lattice quasiholes from density measurements: A tree tensor network study, *Phys. Rev. Res.* **2**, 013145 (2020).
- [76] B. Wang, X.-Y. Dong, and A. Eckardt, Measurable signatures of bosonic fractional Chern insulator states and their fractional excitations in a quantum-gas microscope, *SciPost Phys.* **12**, 095 (2022).
- [77] R. O. Umucal ılar, Bulk density signatures of a lattice quasi-hole with very few particles, *Phys. Rev. A* **108**, L061302 (2023).
- [78] N. Higashino and Y. Tada, Stability of quasiparticle creation and multiband quantum geometry in fractional chern insulators under magnetic fields, *Phys. Rev. B* **111**, 245154 (2025).
- [79] P. J. Ledwith, G. Tarnopolsky, E. Khalaf, and A. Vishwanath, Fractional Chern insulator states in twisted bilayer graphene: An analytical approach, *Phys. Rev. Res.* **2**, 023237 (2020).
- [80] J. Wang, J. Cano, A. J. Millis, Z. Liu, and B. Yang, Exact Landau level description of geometry and interaction in a flatband, *Phys. Rev. Lett.* **127**, 246403 (2021).
- [81] P. J. Ledwith, A. Vishwanath, and D. E. Parker, Vortexability: A unifying criterion for ideal fractional chern insulators, *Phys. Rev. B* **108**, 205144 (2023).
- [82] B. Li and F. Wu, Variational mapping of chern bands to Landau levels: Application to fractional chern insulators in twisted mote_2 , *Phys. Rev. B* **111**, 125122 (2025).
- [83] B. A. Bernevig and N. Regnault, Emergent many-body translational symmetries of Abelian and non-Abelian fractionally filled topological insulators, *Phys. Rev. B* **85**, 075128 (2012).
- [84] E. Ardonne, E. J. Bergholtz, J. Kailasvuori, and E. Wikberg, Degeneracy of non-abelian quantum hall states on the torus:

- domain walls and conformal field theory, *J. Stat. Mech.* **2008**, P04016 (2008).
- [85] S. Johri, Z. Papić, R. N. Bhatt, and P. Schmitteckert, Quasi-holes of $\frac{1}{3}$ and $\frac{7}{3}$ quantum hall states: Size estimates via exact diagonalization and density-matrix renormalization group, *Phys. Rev. B* **89**, 115124 (2014).
- [86] F. D. M. Haldane, Fractional quantization of the hall effect: A hierarchy of incompressible quantum fluid states, *Phys. Rev. Lett.* **51**, 605 (1983).
- [87] F. Wu, T. Lovorn, E. Tutuc, I. Martin, and A. H. MacDonald, Topological insulators in twisted transition metal dichalcogenide homobilayers, *Phys. Rev. Lett.* **122**, 086402 (2019).
- [88] A. M. Läuchli, Z. Liu, E. J. Bergholtz, and R. Moessner, Hierarchy of fractional chern insulators and competing compressible states, *Phys. Rev. Lett.* **111**, 126802 (2013).
- [89] C. Repellin, B. A. Bernevig, and N. Regnault, Z_2 fractional topological insulators in two dimensions, *Phys. Rev. B* **90**, 245401 (2014).
- [90] H. Pan, F. Wu, and S. Das Sarma, Band topology, hubbard model, heisenberg model, and dzyaloshinskii-moriya interaction in twisted bilayer wse_2 , *Phys. Rev. Res.* **2**, 033087 (2020).
- [91] B. I. Halperin, Statistics of quasiparticles and the hierarchy of fractional quantized hall states, *Phys. Rev. Lett.* **52**, 1583 (1984).
- [92] F. D. M. Haldane and E. H. Rezayi, Finite-size studies of the incompressible state of the fractionally quantized hall effect and its excitations, *Phys. Rev. Lett.* **54**, 237 (1985).
- [93] G. Fano, F. Ortolani, and E. Colombo, Configuration-interaction calculations on the fractional quantum hall effect, *Phys. Rev. B* **34**, 2670 (1986).
- [94] R. Morf and B. I. Halperin, Monte carlo evaluation of trial wave functions for the fractional quantized hall effect: Disk geometry, *Phys. Rev. B* **33**, 2221 (1986).
- [95] S. N. Yi, X. M. Chen, and J. J. Quinn, Composite-fermion excitations and the electronic spectra of fractional quantum hall systems, *Phys. Rev. B* **53**, 9599 (1996).
- [96] A. Wójs and J. J. Quinn, Quasiparticle interactions in fractional quantum hall systems: Justification of different hierarchy schemes, *Phys. Rev. B* **61**, 2846 (2000).
- [97] M. Gattu, G. J. Sreejith, and J. K. Jain, Scanning tunneling microscopy of fractional quantum hall states: Spectroscopy of composite-fermion bound states, *Phys. Rev. B* **109**, L201123 (2024).
- [98] H. Q. Trung, Q. Xu, and B. Yang, Long-range entanglement and role of realistic interaction in braiding of non-abelian quasiholes in fractional quantum hall phases (2025), arXiv:2503.13380 [cond-mat.str-el].
- [99] Q. Xu, G. Ji, Y. Wang, H. Q. Trung, and B. Yang, Dynamics of clusters of anyons in fractional quantum hall fluids (2025), arXiv:2505.20257 [cond-mat.str-el].
- [100] V. Crépel, N. Regnault, and R. Queiroz, Chiral limit and origin of topological flat bands in twisted transition metal dichalcogenide homobilayers, *Communications Physics* **7**, 146 (2024).
- [101] R. Roy, Band geometry of fractional topological insulators, *Phys. Rev. B* **90**, 165139 (2014).
- [102] T. S. Jackson, G. Möller, and R. Roy, Geometric stability of topological lattice phases, *Nature Communications* **6**, 8629 (2015).
- [103] Z. Liu, B. Mera, M. Fujimoto, T. Ozawa, and J. Wang, Theory of generalized landau levels and implication for non-abelian states (2024), arXiv:2405.14479 [cond-mat.mes-hall].
- [104] Y. Qian, T. Zhao, J. Zhang, T. Xiang, X. Li, and J. Chen, Describing landau level mixing in fractional quantum hall states with deep learning, *Phys. Rev. Lett.* **134**, 176503 (2025).
- [105] Y. Teng, D. D. Dai, and L. Fu, Solving the fractional quantum hall problem with self-attention neural network, *Phys. Rev. B* **111**, 205117 (2025).
- [106] X. Li, Y. Chen, B. Li, H. Chen, F. Wu, J. Chen, and W. Ren, Deep learning sheds light on integer and fractional topological insulators (2025), arXiv:2503.11756 [cond-mat.str-el].
- [107] D. Luo, T. Zaklana, and L. Fu, Solving fractional electron states in twisted $mote_2$ with deep neural network (2025), arXiv:2503.13585 [cond-mat.str-el].
- [108] X.-Y. Song and T. Senthil, Density wave halo around anyons in fractional quantum anomalous hall states, *Phys. Rev. B* **110**, 085120 (2024).